Structure refinement from precession electron diffraction data

Lukáš Palatinus,[a]* Damien Jacob,[b] Priscille Cuvillier,[b] Mariana Klementová,[a] Wharton Sinkler[c] and Laurence D. Marks[d]

[a]Institute of Physics of the AS CR, v.v.i., Na Slovance 2, 182 21 Prague, Czech Republic, [b]Unité Matériaux et Transformations, Université Lille 1, CNRS UMR 8207, 59655 Villeneuve d'Ascq, France, [c]UOP LLC, a Honeywell Company, Des Plaines IL 60017, USA, and [d]Department of Materials Science and Engineering, Northwestern University, Evanston IL 60201, USA. Correspondence e-mail: palat@fzu.cz

Electron diffraction is a unique tool for analysing the crystal structures of very small crystals. In particular, precession electron diffraction has been shown to be a useful method for *ab initio* structure solution. In this work it is demonstrated that precession electron diffraction data can also be successfully used for structure refinement, if the dynamical theory of diffraction is used for the calculation of diffracted intensities. The method is demonstrated on data from three materials – silicon, orthopyroxene $(Mg,Fe)_2Si_2O_6$ and gallium–indium tin oxide $(Ga,In)_4Sn_2O_{10}$. In particular, it is shown that atomic occupancies of mixed crystallographic sites can be refined to an accuracy approaching X-ray or neutron diffraction methods. In comparison with conventional electron diffraction data, the refinement against precession diffraction data yields significantly lower figures of merit, higher accuracy of refined parameters, much broader radii of convergence, especially for the thickness and orientation of the sample, and significantly reduced correlations between the structure parameters. The full dynamical refinement is compared with refinement using kinematical and two-beam approximations, and is shown to be superior to the latter two.

1. Introduction

Electron microscopy, spectroscopy and diffraction are indispensable tools for the characterization of crystalline materials. They can provide local information from crystals as small as a few nanometres. With the advent of aberration-corrected transmission electron microscopes, the direct imaging provides ever-improving atomic resolution images of crystal structures. However, while one can correct the imaging aberrations optically, one cannot correct for dynamical diffraction effects.

Within an electron microscope, electron diffraction remains the most accurate and versatile method of obtaining accurate structural information at the atomic level, although imaging experiments are in some cases starting to approach comparable accuracies. Consequently there have been many attempts to use electron diffraction as a quantitative tool, dating back to the earliest days when microscopes had very limited resolutions for imaging but were good diffraction cameras. Much of the early work is discussed in the books by Vainshtein (1964), Cowley (1992), Spence & Zuo (1992) and Dorset (1995). In many cases fully quantitative analyses proved difficult because of the complications of dynamical diffraction. In some cases this has been approached directly as for convergent-beam electron diffraction (CBED) or low-energy electron diffraction (LEED); indeed LEED has for many years been the dominant technique for solving surface structures. More often diffraction data have been used in a qualitative or only semi-quantitative fashion, for instance in the solution of the Si (111) 7 × 7 surface (Takayanagi *et al.*, 1985; Gilmore *et al.*, 1997), nanotubes (Iijima, 1991; Zhang *et al.*, 1993) or for super-structures and incommensurate structures (*e.g.* Steeds *et al.*, 1985), where it is necessary to obtain diffraction data from only local regions.

An important method for structure analysis of nanocrystals is quantitative modeling of CBED data. CBED is an excellent technique for refining accurate low-angle structure factors and for gaining insight into the charge-density distribution in the crystal (Zuo & Spence, 1991; Spence, 1993; Zuo *et al.*, 1993; Cheng *et al.*, 1996; Nuchter *et al.*, 1998; Cao *et al.*, 2009). Several papers have investigated the refinement of structural parameters using this technique (Tsuda & Tanaka, 1999; Tsuda *et al.*, 2002, 2010; Ogata *et al.*, 2004; Feng *et al.*, 2005), often in connection with the refinement of a few low-order structure factors. The works are, however, so far limited to relatively simple structures.

There has recently been a resurgence of interest in quantitative analysis of high-energy electron diffraction data due to the introduction of the precession electron diffraction (PED) technique (Vincent & Midgley, 1994). Key to this was the demonstration by Gjønnes and collaborators (Berg *et al.*, 1998;

 171

Gjønnes et al., 2003) that PED data could be used within direct methods rather well, and also used at least partially to refine a structure. While it was apparent from the early days that PED remained somewhat dynamical and needed a full dynamical calculation for quantitative results (Own, 2005; Own et al., 2006), numerous groups have reported reasonable results with approximate kinematical refinements (Mugnaioli et al., 2009; Hadermann et al., 2010; Birkel et al., 2010; Rozhdestvenskaya et al., 2010; White et al., 2010; Gemmi et al., 2010, 2012; Palatinus et al., 2011; Klein, 2011). The reason for this is that PED is pseudo-kinematical with reflections with large structure factors tending to have large intensities, what has been referred to as intensity ordering (Marks & Sinkler, 2003). In a sense, successes to date are similar to the earliest days of X-ray diffraction when both direct methods and refinements could be performed using approximate decompositions of the intensities into those which were 'strong', 'intermediate' or 'weak'.

Several groups have worked on full dynamical refinement of non-precessed spot electron diffraction patterns and there are several computer programs available for this purpose: *Numis* (Marks et al., 1993), *EDM* (Kilaas et al., 2005), *MSLS* (Jansen et al., 1998), *ASTRA* (Dudka, 2007), *eSlice* (Oleynikov, 2011). To our knowledge, however, so far only one dynamical structure refinement against PED data has been reported (Dudka et al., 2008). The refinement was performed against one zone-axis pattern of silicon [110], and very few details about the refinement characteristics, reliability and reproducibility were reported. The purpose of this paper is to demonstrate that PED data can be used successfully for accurate structure refinement. We provide results on three different materials and several data sets measured with three different microscopes. We analyze the sensitivity of the results to the choice of the parameters of the algorithms. The differences between the full dynamical refinement, a simplified two-beam dynamical refinement and the simplest approximation of kinematical diffraction are analyzed, and the results are compared with refinement against non-precessed electron diffraction data.

2. Samples and experimental data

2.1. Silicon

Silicon is often used as a standard for testing new methods in materials science. Its advantages are a very small unit cell and few parameters. For our experiment we used a silicon standard sample MAG*I*CAL (Electron Microscopy Sciences), which provides a wedged sample of silicon cut perpendicular to the [110] zone axis. The angle of the wedge is very small and small areas of the sample can be considered as essentially parallel slabs. The data were collected on a Philips CM120 transmission electron microscope equipped with a 14-bit wide-angle charge-coupled device (CCD) camera OSIS Veleta and NanoMEGAS Digistar precession device. The accelerating voltage was 120 kV. Data were collected at four different spots with different thicknesses, and at each spot the
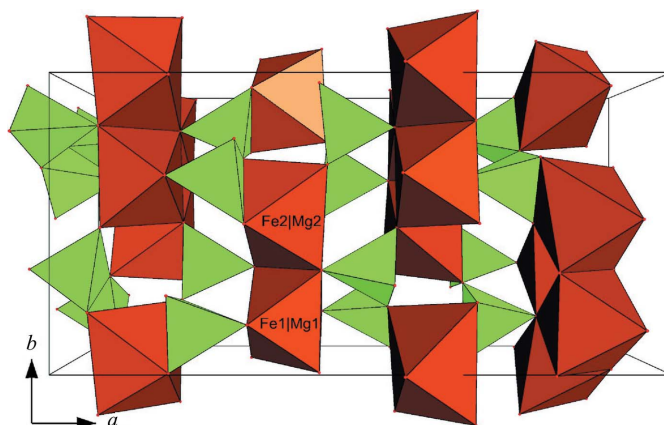
Figure 1
Structure of orthopyroxene viewed along **c**. Double chains of Fe/Mg-containing octahedra alternate with simple chains of SiO_4 tetrahedra. All octahedra contain sites with mixed Fe/Mg occupancy. Two independent octahedra are labeled with atomic labels that are referred to in the text and tables.

intensities were measured with precession angles φ of 0, 1, 2 and 3°. On the first spot the diffraction was measured in the selected-area (SA) mode, with the radius of the SA aperture 300 nm and with negligible beam divergence (<0.2 mrad); the remaining three spots were measured in a microdiffraction mode, with the spot size 100 nm and beam convergence angle 1.35 mrad.
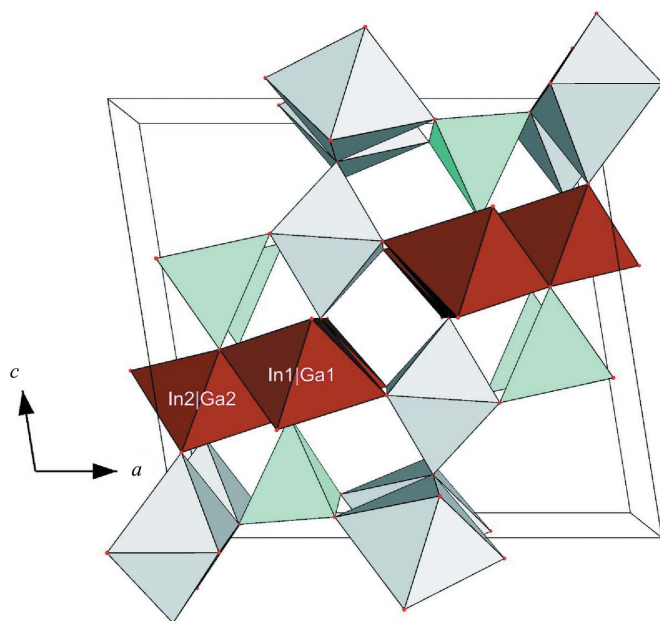
2.2. Orthopyroxene

Orthopyroxene is an Fe–Mg-bearing silicate mineral from the group of pyroxenes, with a structure formed by chains of SiO_4 tetrahedra linked together by FeO_6 octahedra (Fig. 1). Pyroxenes are important rock-forming minerals which often contain sites with mixed occupancies. The distribution of cations in these sites can be used as a geothermometer (Stimpfl et al., 1999). Because the mineral often forms very small grains, electron diffraction is an attractive method for their analysis, provided it allows the determination of the occupancies with sufficient accuracy. The possibility of using PED data for this purpose was demonstrated in a dedicated paper (Jacob et al., 2013) using grid-search methods. In this work we use the same data sets for structure refinements.

We measured data from two samples: an ordered one (natural, non-treated) and a disordered one (heat-treated). Samples were monocrystals of natural $(Mg_xFe_{1-x})_2Si_2O_6$ orthopyroxenes (a few hundred microns in size) from granulite rocks of the Wilson Terrane, North Victoria Land, Antarctica (Tarantino et al., 2002). The average crystal composition as obtained by electron microprobe corresponds to x close to 0.7. In order to obtain disordered structures, crystals of the same origin were heated for 48 h at 1273 K. For details of the treatment see Jacob et al. (2013). Both samples were analyzed on a single-crystal X-ray diffractometer following the experimental procedure described in Tarantino et al. (2002). Then a thin slab of the sample with thickness

around 40–50 nm was cut from the crystals perpendicular to the [001] direction using a focused ion beam. TEM (transmission electron microscopy) observations were performed on an FEI Tecnai G^2 20 operated at 200 kV and equipped with a NanoMEGAS Digistar precession device. SA electron diffraction patterns were obtained using a defocused parallel beam (beam convergence angle <0.3 mrad) and a circular aperture selecting an illuminated area of about 250 nm in diameter. Microdiffraction patterns were obtained using a probe of about 10–40 nm in diameter produced by a 10 μm condenser aperture, with beam convergence approximately 1.7 mrad. Several diffraction patterns were collected from different positions on the sample using precession angles φ of 0, 1.6 (treated sample only), 2.4 and 2.8°. Small-spot illumination was used to collect the data sets oplt1Ap2.4, oplt1Ap2.8 and oplt1Bp2.8 (see §2.4 for an explanation of the numbering of the data sets). All other data sets were collected using SA electron diffraction.

2.3. Gallium–indium tin oxide

Gallium–indium tin oxide (GITO) forms an interesting channel structure formed by Sn-containing octahedra and Ga-containing tetrahedra alternating with two octahedra with mixed gallium/indium occupancy (Fig. 2). The structure was solved from a combination of high-resolution transmission electron microscopy (HRTEM) imaging and an electron diffraction pattern of the [010] zone axis, and later refined against neutron powder diffraction data (Sinkler *et al.*, 1998; Edwards *et al.*, 2000). We used electron diffraction data from a

Table 1
Basic crystallographic information about the samples.

	Silicon	Orthopyroxene	GITO
Composition	Si	$(Fe,Mg)SiO_3$	$Ga(Ga,In)SnO_5$
a (Å)	5.431	18.268	11.689
b (Å)	5.431	8.868	3.167
c (Å)	5.431	5.202	10.731
α (°)	90	90	90
β (°)	90	90	99.00
γ (°)	90	90	90
V_{UC} (Å^3)	160.15	842.73	392.36
Space group	$Fd\bar{3}m$	$Pbca$	$P2/m$
Reference	Többens *et al.* (2001)	Jacob *et al.* (2013)	Edwards *et al.* (2000)
Measured zone	[011]	[001]	[010]
No. of reflections ($g < 1.4$ Å^{-1})	58	484	694

sample with composition $(Ga_{2.8}In_{1.2})Sn_2O_{10}$. The sample was prepared by crushing the raw material to a fine powder and dispersing it on a TEM grid. The oriented diffraction pattern of the [010] zone was collected at an accelerating voltage of 200 kV using a Jeol 2000FX transmission electron microscope equipped with a Gatan Ultrascan 1000 CCD camera. The data were collected using small-spot illumination with an almost parallel beam (beam convergence <0.3 mrad) and spot diameter of about 100 nm. One data set was collected with precession angle $\varphi = 1.375°$ and one without precession.

2.4. Data processing

All experimental diffraction patterns were processed using the program *PETS* (Palatinus, 2011). The output of the program is a list of reflections with their indices, intensities on an arbitrary scale and estimated standard deviations (e.s.d.'s) of the intensities $\sigma(I)$. To estimate the e.s.d.'s, Poisson statistics were assumed for the diffraction signal, and the background of the images was analyzed to estimate the contribution of the detector noise to the variance of individual pixel counts. Details of the data-processing procedure are described in Appendix A. Intensities were extracted up to $g_{max} = 1.4$ Å^{-1}. Examples of diffraction patterns are shown in Fig. 3.

The basic crystallographic information about all three samples is summarized in Table 1. Throughout this paper the data sets are labeled with a code of the sample (si: silicon; opht: treated orthopyroxene sample; oplt: natural orthopyroxene sample; gito: gallium–indium tin oxide) followed by the number of the spot and indication of the precession angle. As an example, si3p2.0 is the silicon data set from the spot number 3 taken with $\varphi = 2.0°$. For the natural orthopyroxene, several data sets were collected from some spots. These data sets are distinguished by a capital letter following the spot number, *e.g.* oplt1Bp2.4.

3. Computational aspects

3.1. Calculation of dynamical intensities

The diffraction of electrons by a crystal is described by the dynamical theory of diffraction. The diffracted intensities are

Figure 2
Structure of gallium indium tin oxide (GITO) viewed along **b**. Chains of corner-sharing GaO$_4$ tetrahedra (light blue) alternate with chains of edge-sgaring SnO$_6$ octahedra (grey) and with double chains of edge-sharing octahedra (dark red) that contain mixed In/Ga sites. Two independent octahedra are labeled with atomic labels that are referred to in the text and tables.

commonly calculated by one of two methods. In the multislice method (Cowley & Moodie, 1957; Self & O'Keefe, 1988), a numerical integration of the scattering and propagation of the electron wave is performed. The second method is the method of Bloch waves due to Bethe (1928) and Humphreys (1979), which is based on a solution of the Schrödinger equation for high-energy electrons. The approaches have been shown to be equivalent if the calculations are performed to sufficient accuracy. The multislice method is generally faster for the typical thicknesses of TEM samples and larger unit cells.

Nevertheless, in this work we opt for the Bloch-wave formalism. The main reason is that the Bloch-wave method provides closed-form expressions for the intensities and can thus be treated analytically. In particular, it is possible to find analytical derivatives of the intensities with respect to the structure parameters. Moreover, it has been shown (Sinkler & Marks, 2010) that the properties of the mathematical expression of the method allow for a simultaneous calculation of the intensities at several orientations of the incident beam, allowing also for a significant speed up of the calculation of the
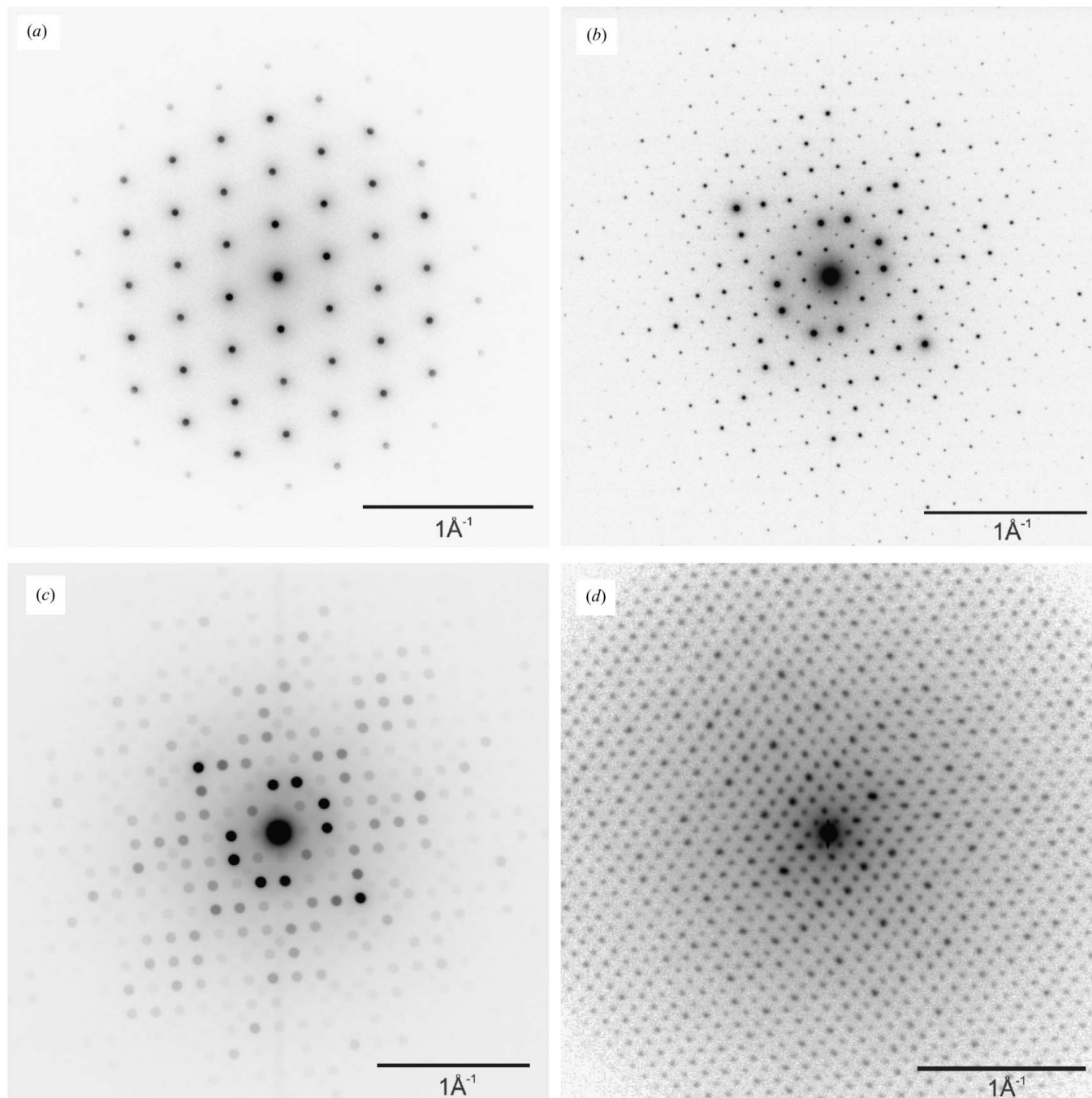
Figure 3
Selected experimental diffraction patterns. Intensities are shown on logarithmic scale to emphasize the weak background. (a) si3p1.0, (b) opht2p1.6, (c) oplt1Ap2.8, (d) gito1p1.4.

PED intensities. The present work is focused on a 'proof of principle' of the refinement procedure and it does not aim at the optimization of the computing time. Therefore it does not exploit any of these advanced possibilities offered by the Bloch-wave method. However, it will serve as a reference for future work, which will focus on the optimization of the computing time.

As a reference for the implementation of the Bloch-wave method we used the formalism described in Hirsch *et al.* (1977) (see also Spence & Zuo, 1992, §3.2). Because it is central for this work, we briefly repeat here the basic procedure. In the first step the structure matrix $\mathbf{A}$ is constructed:

$$a_{ii} = 2KS_{\mathbf{g}_i}, \quad i = 1, N_{\text{beams}},$$
$$a_{ij} = U_{\mathbf{g}_i - \mathbf{g}_j}, \quad i, j = 1, N_{\text{beams}}; \; i \neq j. \tag{1}$$

Here K is the length of the wavevector of the incident beam corrected for the mean inner potential in the crystal, $S_{\mathbf{g}}$ is the excitation error of the beam $\mathbf{g}$, *i.e.* the signed distance of the reciprocal-lattice node from the Ewald sphere measured along the surface normal, and $U_{\mathbf{g}}$ are quantities defined as $U_{\mathbf{g}} = 2meV_{\mathbf{g}}/h^2$, where $V_{\mathbf{g}}$ is the Fourier component of the electrostatic potential in the crystal.

Next, the eigenvector equation $\mathbf{AC} = \mathbf{C}[\lambda]$ is solved to obtain the matrix $\mathbf{C}$ of the eigenvectors and the diagonal matrix $[\lambda]$ of the eigenvalues of the matrix $\mathbf{A}$. Then the scattering matrix $\mathbf{S}$ is constructed as $\mathbf{S} = \mathbf{C}[\tau]\mathbf{C}^{-1}$. In this expression $[\tau]$ is a diagonal matrix with elements

$$\tau_{jj} = \exp\left[\frac{\pi i t \lambda_{jj}}{(\mathbf{K} + \mathbf{g}_j) \cdot \mathbf{n}}\right], \tag{2}$$

where $\mathbf{n}$ is the normal to the sample surface pointing towards the source of electrons and t is the sample thickness. If we set up the structure matrix $\mathbf{A}$ such that $\mathbf{g}_1 = 0$, then the intensities of the beams are found as the moduli squared of the elements in the first column of the scattering matrix:

$$I_{\mathbf{h}_i} = |s_{i1}|^2. \tag{3}$$

This equation neglects the contribution to the intensity $I_{\mathbf{h}_i}$ from different Bloch waves with the same projection of the wavevector on the surface normal. For example, if the surface normal is parallel to the zone [001], beams with fixed indices h and k and variable l will all superimpose and interfere coherently. Thus, the correct expression for the measured intensity of beam $\mathbf{h}_i$ is given by

$$I_{\mathbf{h}_i} = \left|\sum_j s_{j1}\right|^2, \tag{4}$$

where the summation runs over all indices j such that the projections of $\mathbf{h}_j$ and $\mathbf{h}_i$ on the surface plane are equal. This effect is very small for structures with small unit cells, where the higher-order reflections have very large excitation errors and consequently contribute very little to the scattering. For the examples considered in this work, the excitation errors needed for including the higher-order beams in the sum were much larger than the limits used in the calculation and this

effect could therefore be ignored. However, it might be necessary to consider it for more complex structures with larger unit cells.

The computation procedure is controlled by five crystal- and orientation-related parameters (experimental parameters for brevity) and by the parameters influencing the selection of the beams forming the matrix $\mathbf{A}$ (in short, computation parameters). The five experimental parameters are the thickness, the orientation of the incident beam (or of the center of the precession circuit) with respect to the crystal lattice (two parameters) and the orientation of the surface normal with respect to the crystal lattice (two parameters). The contribution of a particular beam to the diffracted intensities increases, in general, with increasing amplitude of its structure factor and with decreasing excitation error $S_{\mathbf{g}}$. The amplitudes of the structure factors decrease rapidly with the length of the associated reciprocal-lattice vector. The selection of the beams for the calculation can thus be governed by two computation parameters: the maximal excitation error $S_{\mathbf{g}}^{\max}$ and the maximum length of the diffraction vector $g^{\max}$. For a given orientation of the crystal and of the surface normal, these two parameters uniquely define the selection of the beams. To save computing time, part of the beams can be excluded from the diagonalization and treated using Bethe potentials (Zuo & Weickenmeier, 1995). This is undoubtedly an efficient way of improving the accuracy of the calculation while saving computing time. However, in this work we did not make use of perturbation theory and all beams were included in the diagonalized matrix. We also assumed that the sample surface is perpendicular to the zone axis and we are implicitly using the column approximation. Furthermore, we neglected absorption effects on the diffracted intensities to reduce the computing time. It is likely that including absorption effects would further improve the fit, but our test calculations (§5) indicate that the improvement would probably not be dramatic.

The tradition in electron diffraction has been to collect oriented patterns of some principal plane, *i.e.* with the incident beam parallel to some zone axis with low indices. Deviations from the exact orientation are described as the tilt of the incident beam with respect to the zone axis. Often this is a useful concept, but it is by no means required by the formalism outlined above. A more general approach is to assume an arbitrary orientation of the crystal defined by the orientation matrix with respect to the microscope's coordinate system. The excitation error of every beam can be calculated using the orientation matrix and the surface normal alone, and the concept of zone axis is not necessary anymore. As a result, this implementation can be used to calculate intensities on an oriented plane and of a completely arbitrary orientation on the same footing. No distinction has to be made between reflections belonging to the zero-order Laue zone (ZOLZ) and higher-order Laue zones (HOLZs).

In PED the beam performs a precessing motion. The integrated diffracted intensities should be calculated as an integral over the intensities diffracted at every possible orientation of the incident beam. The integration is performed numerically

as a sum of the intensities calculated at a finite number of orientations N_{or} along the precession circuit. The finer is the sampling, the more accurate is the result. N_{or} is thus an additional computation parameter of the method in the case of PED.

3.2. Refinement procedure

For the least-squares refinement procedure we employed the standard Gauss–Newton algorithm with parameter shifts determined by line search. This simple approach is sufficient for small residual problems, where the initial point is close to the solution, although there are of course better and more robust methods in the mathematics literature for more complicated problems. The derivatives were calculated by central finite differences. The figures of merit traditionally used to assess the match between the calculated and experimental data are the R values. In this work we use three well established types of R values, that we list here for reference:

$$wR2 = \left[\frac{\sum w_{\mathbf{g}} \left(I_{\mathbf{g}}^{o} - I_{\mathbf{g}}^{c} \right)^2}{\sum w_{\mathbf{g}} \left(I_{\mathbf{g}}^{o} \right)^2} \right]^{1/2}, \qquad (5)$$

$$R2 = \frac{\sum \left| I_{\mathbf{g}}^{o} - I_{\mathbf{g}}^{c} \right|}{\sum \left| I_{\mathbf{g}}^{o} \right|}, \qquad (6)$$

$$R1 = \frac{\sum \left| (I_{\mathbf{g}}^{o})^{1/2} - (I_{\mathbf{g}}^{c})^{1/2} \right|}{\sum (I_{\mathbf{g}}^{o})^{1/2}}. \qquad (7)$$

In the above formulae $I_{\mathbf{g}}^{o}$ and $I_{\mathbf{g}}^{c}$ are the observed and calculated intensities of the beam $\mathbf{g}$, respectively, $w_{\mathbf{g}} = \sigma^{-2}(I_{\mathbf{g}}^{o})$, and the summations run over all reflections from the experimental data set. The first R value, $wR2$, is proportional to the square root of the minimized function in the least-squares procedure. $R2$ is an R value on diffracted intensities, while $R1$ is calculated on diffracted amplitudes. $R1$ is the value traditionally used in X-ray crystallography to assess the quality of the match between experimental and calculated data sets.

The only parameters that did not yield a smooth dependence of the minimized function on the variation of the parameters were the two parameters defining the orientation of the crystal with respect to the center of the precession circuit (Fig. 4). The dependence is relatively well behaved, with one clear minimum. However, the function is not smooth in detail. This can be easily understood. If the orientation changes, the excitation error of all reflections changes too and, therefore, the matrix $\mathbf{A}$ can contain a different set of reflections. Consequently, the calculated intensities can undergo abrupt changes during continuous tilting of the crystal. The changes are small if the set of reflections included in $\mathbf{A}$ is sufficiently large, but for all realistic sets of reflections they are sufficient to prevent a smooth dependence of the minimized function on the orientation parameters. It is thus necessary to perform some kind of grid search to find the best orientation.

Because of the generally well defined minimum it is not necessary to perform a full grid search. Instead we adopted the following protocol, which is similar to a simplex method. The
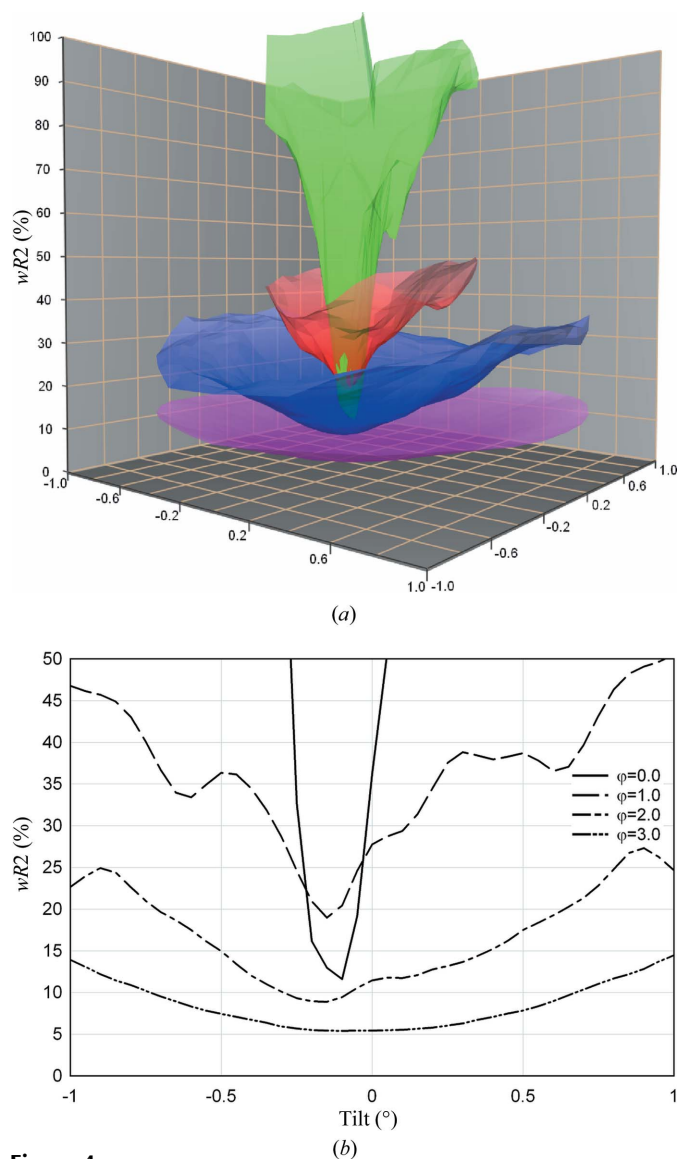
Figure 4
$wR2$ as a function of the tilt from an ideal zone-axis orientation calculated on the data sets si2p0.0, si2p1.0, si2p2.0 and si2p3.0. (a) Surface plot. (b) Section of the surface plot passing through zero and through the minimum of the surface for $\varphi = 0$.

tilt is described by two Euler angles: φ (rotation around the z axis) and θ (rotation around the new x axis). Thus, φ defines the direction of the tilt and θ its amplitude. The zero values of the two angles correspond to the original orientation of the crystal as defined by the orientation matrix. The new orientation is searched at values $\theta = \theta_{search}$, $\varphi = n \times 60°$, $n = 0, \ldots, 5$, i.e. in a hexagon around the original orientation. At each orientation the value of $wR2$ is calculated. If any of the new orientations yields a lower value of $wR2$, the crystal orientation is updated and the search is repeated from the new orientation with the same θ_{search}. Otherwise θ_{search} is divided by two and the search is repeated from the same orientation on a finer grid. The procedure is repeated until a predefined minimum value of θ_{search}^{min} is reached. The values of θ_{search}^{min} and θ_{search}^{max} are functions of the precession angle. For small or zero precession angle, the minimum in the function is very narrow

and deep. It is therefore necessary to do a very fine search (small $\theta_{\text{search}}^{\min}$) to find the real minimum. On the other hand, for large precession angles the minimum is broad. It is possible to converge to the correct minimum even from a relatively poor initial guess, and it is not necessary to sample the function too finely. For large precession angles, $\theta_{\text{search}}^{\min}$ and $\theta_{\text{search}}^{\max}$ can thus be relatively large. Based on the plots in Fig. 4 we decided to use the following empirical formula for $\theta_{\text{search}}^{\min}$ as a function of the precession angle:

$$\theta_{\text{search}}^{\min} = 0.02 + 0.02\varphi, \qquad (8)$$

with $\theta_{\text{search}}^{\min}$ and the precession angle φ expressed in degrees. $\theta_{\text{search}}^{\max}$ is set to $8 \times \theta_{\text{search}}^{\min}$, so that θ_{search} attains four consecutively smaller values during the search.

The complete refinement protocol is thus the following:

(i) Perform an initial orientation grid search and a search for the optimum thickness.

(ii) Refine the selected parameters until convergence. For the purposes of this work the refinement was considered converged if the maximal parameter change divided by its e.s.d. was below 0.1.

(iii) Perform a new orientation search.

(iv) If the orientation search found a better orientation, update the orientation and return to point (ii). Otherwise stop the refinement procedure.

We note that a similar approach, notably the separation of the orientation and thickness optimization from other parameters, was also used in the context of the refinement of CBED diffraction patterns (Zuo, 1993) or for dynamical refinement of surface diffraction data (Marks *et al.*, 1993).

3.3. Alternative refinement models

In the current crystallographic literature the structures determined from PED data are sometimes refined using the kinematical approximation. In this approximation the intensities are considered to be proportional to the square of the structure-factor amplitude:

$$I_{\mathbf{g}}^{\text{kin}} \propto |U_{\mathbf{g}}|^2. \qquad (9)$$

This approximation is inadequate, but often yields stable refinement. However, the accuracy of the refined parameters cannot be estimated because the underlying model is not appropriate and, therefore, the estimated standard deviations derived from the least-squares procedure are not reliable. We performed a kinematical refinement on all data sets and we compare the results with the full dynamical calculations.

Another possible model is the two-beam refinement proposed by Sinkler *et al.* (2007). This technique can be considered as an intermediate step between the kinematical model and the full dynamical model. In the two-beam model the intensity of each reflection is calculated using dynamical diffraction theory, but neglecting the contribution of all other beams except for the incident beam. The intensity in the two-beam approximation can be calculated as (Hirsch *et al.*, 1977; Spence & Zuo, 1992)

$$I_{\mathbf{g}}^{\text{tb}} = |U_{\mathbf{g}}|^2 \frac{\sin^2\left\{[\pi t/(\mathbf{K} \cdot \mathbf{n})](K^2 S_{\mathbf{g}}^2 + |U_{\mathbf{g}}|^2)^{1/2}\right\}}{K^2 S_{\mathbf{g}}^2 + |U_{\mathbf{g}}|^2}. \qquad (10)$$

It was shown in the work of Sinkler *et al.* (2007) that the two-beam model yields better agreement with simulated dynamical diffraction data than the kinematical model. We compare the two-beam refinement with other refinement models using experimental data.

3.4. Software

All calculations in this work have been performed using a dedicated piece of software written for this purpose. The core of the software is the Bloch-wave calculation. This part was written with the help of the code `bethe_n` by Wharton Sinkler (unpublished software, used as a basis for the article Sinkler & Marks, 2010) and the results were cross-checked with this code. Furthermore, the correctness of the implementation was cross-checked also against the computing system *JEMS* (Stadelmann, 2004). The intensities calculated for the ortho-pyroxene structure were also compared with the results of the multislice calculations using the program *Numis* (Marks *et al.*, 1993). For $\varphi = 36$ mrad (2.06°) and thickness 520.2 Å (100 unit cells), an $R2$ value of 0.50% was obtained. We attribute the remaining discrepancy to the different ways the two calculations handle the HOLZ effects and to the limited number of beams that can be included in the Bloch-wave calculation. All the calculations in this work used the analytical fit to atomic scattering factors due to Weickenmeier & Kohl (1991).

## 4. Results

4.1. Choice of the computation parameters

Before the actual structure refinement against individual data sets, it was necessary to analyze the influence of the parameter selection on the result and determine the optimal values of the computation parameters for the final refinement. The parameters to be determined are $S_{\mathbf{g}}^{\max}$, $g^{\max}$ and N_{or}. One way of assessing the influence of the parameters on the calculated intensities is to calculate a series of simulated data sets with various settings and compare them with the best available estimate of the 'true' intensities. To estimate the effect of the choice of N_{or}, we calculated a set of intensities for silicon for $\varphi = 1.0$ and 3.0°, and thicknesses of 40 and 110 nm. N_{or} ranged from 48 to 576, and 576 was already sufficiently fine to be taken as a good approximation to the true values, to which other calculations can be related. Fig. 5 shows a plot of $R2$ values between individual data sets and the data sets calculated with $N_{\text{or}} = 576$. It can be seen that for a small precession angle and/or small thickness, fairly low N_{or} values around 200 or less are sufficient for accurate calculation, while for a thick sample and large precession angle values over 500 are necessary.

The influence of the parameters $S_{\mathbf{g}}^{\max}$ and $g^{\max}$ on the diffracted intensities were analyzed in the past (Zuo & Weickenmeier, 1995) on simulated data of MgO and GaP.
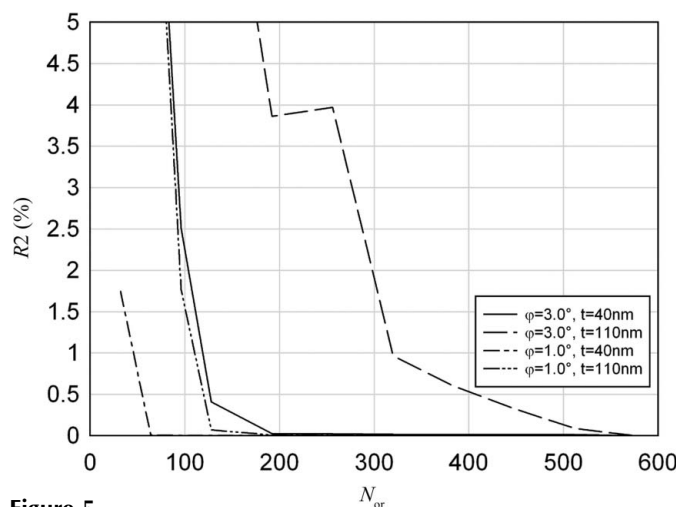
Figure 5
Convergence of Bloch-wave calculations for silicon [110] with increasing N_{or}. Horizontal axis: N_{or}, vertical axis: $R2$ with respect to the largest calculation with $N_{or} = 576$.

Here we checked these parameters in a similar way, but on more complex structures and against both simulated and experimental data. Calculations on silicon with two thicknesses, on the orthopyroxene structure and on GITO were performed. The 'true' intensities were approximated by intensities calculated with $S_{\mathbf{g}}^{max} = 0.075$ Å^{-1} and $g^{max} = 3.5$ Å^{-1}. The contour plots of $wR2$ values of various parameter choices are shown in the top rows of Figs. 6 and 7. It follows from the images that obtaining quantitative agreement (say $wR2$ below 0.5%) requires very high $S_{\mathbf{g}}^{max}$, around 0.06 Å^{-1} for silicon, 0.04 Å^{-1} for the orthopyroxene calculation and at least 0.07 Å^{-1} for GITO. The value g^{max} is sensitive to the thickness and presence of heavy atoms. A value around 2.0 Å^{-1} is
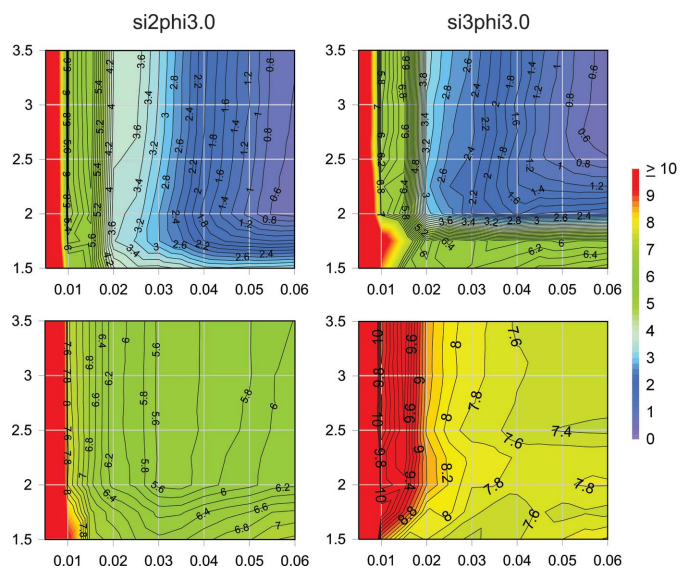
satisfactory for the thin silicon sample and orthopyroxene, while 2.5 Å^{-1} is a minimum for the thick silicon sample and 3.5 is necessary for GITO.

Adopting directly the values estimated in the previous paragraph would lead to very large calculations and consequently to unfeasibly long computing times. It should be noted, however, that the $wR2$ values of the simulations against 'true' data do not transfer directly into the same increase of $wR2$ of experimental data against the simulation. Denoting $wR2$ of a simulation against the truth by R_{st}, $wR2$ of the experimental data against the truth as R_{et} and $wR2$ of the experimental data against the simulation as R_{es}, it can be shown by simple algebraic manipulations of equation (4) that if the deviations of experimental and simulated intensities from the truth are mutually uncorrelated, then

$$R_{es} \simeq (R_{et}^2 + R_{st}^2)^{1/2}. \tag{11}$$

Consequently, using for example computation parameters resulting in $R_{st} = 0.3R_{et}$ will increase R_{es} roughly by a factor of 0.05. The bottom rows of Figs. 6 and 7 demonstrate the effect. These figures show $wR2$ values of the simulations against experimental data. Clearly, the onset of the plateau of essentially constant values is at much smaller parameters than between simulations and the truth. The evaluation of the optimal parameters is complicated by the influence of the experimental noise and uncertainty about the exact structure parameters. This is most notable for the plot for GITO, where there is a clear minimum on the graph for $S_{\mathbf{g}}^{max}$ around 0.02 Å^{-1}, and for higher values $wR2$ slightly increases. For orthopyroxene we can see an oscillation of $wR2$ values with the first minimum at $S_{\mathbf{g}}^{max} = 0.01$ Å^{-1} followed by two small
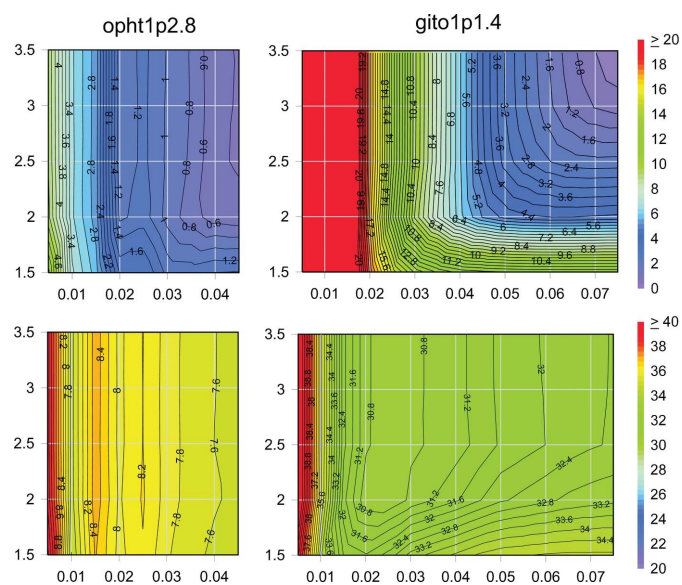

Figure 6
Convergence of Bloch-wave calculations for silicon [110] as a function of g_{max} and $S_{\mathbf{g}}^{max}$. Horizontal axis: $S_{\mathbf{g}}^{max}$, vertical axis: g_{max}. Color code and contours: $wR2$ with respect to the calculation with $S_{\mathbf{g}}^{max} = 0.075$ Å^{-1} and $g_{max} = 3.5$ Å^{-1} (upper row) and with respect to experimental data (lower row).

Figure 7
Convergence of Bloch-wave calculations for gito1p1.4 and opht1p2.8 as a function of g_{max} and $S_{\mathbf{g}}^{max}$. Horizontal axis: $S_{\mathbf{g}}^{max}$, vertical axis: g_{max}. Color code and contours: $wR2$ with respect to the calculation with $S_{\mathbf{g}}^{max} = 0.075$ Å^{-1} and $g_{max} = 3.5$ Å^{-1} (upper row) and with respect to experimental data (lower row). Color scale for the opht1p2.8 data set as in Fig. 6.

Table 2
Results of test refinements on the silicon data set si2p1.0 with various parameters of the Bloch-wave calculation.

Default parameter values: $S_g^{max} = 0.03$ Å^{-1}, $g_{max} = 2.5$ Å^{-1}, $N_{or} = 150$. N_{beams}^{min} and N_{beams}^{max} are the minimum and maximum number of beams that occurred in the structure matrix $\mathbf{A}$ during the N_{or} individual calculations.

Varied parameter	$wR2$ (%)	$R2$ (%)	$R1$ (%)	Thickness (Å)	U(Si) (Å^2)	N_{beams}^{min}	N_{beams}^{max}
Variable S_g^{max}							
0.010	14.96	10.15	12.57	47.73 (124)	0.0056 (27)	24	32
0.015	14.66	9.91	8.93	48.39 (125)	0.0122 (28)	33	44
0.020	14.66	10.61	9.34	48.13 (117)	0.0129 (24)	44	51
0.025	14.59	9.99	8.93	48.73 (122)	0.0159 (26)	52	63
0.030	14.63	10.10	8.94	49.03 (122)	0.0170 (26)	64	73
0.035	14.68	10.22	8.96	49.21 (122)	0.0178 (25)	74	84
0.040	14.76	10.99	9.26	48.56 (117)	0.0162 (23)	82	93
Variable g_{max}							
1.5	15.00	10.38	9.38	50.00 (136)	0.0170 (28)	49	56
2.0	14.63	10.10	8.94	49.06 (123)	0.0171 (26)	64	72
2.5	14.63	10.10	8.94	49.03 (122)	0.0170 (26)	64	73
3.0	14.63	10.10	8.94	49.03 (122)	0.0170 (26)	64	73
3.5	14.67	10.18	8.96	49.01 (123)	0.0169 (26)	74	92
4.0	14.64	10.05	8.93	49.48 (125)	0.0173 (26)	118	131

Table 3
Results of test refinements on the silicon data set si3p3.0 with various parameters of the Bloch-wave calculation.

Default parameter values: $S_g^{max} = 0.03$ Å^{-1}, $g_{max} = 2.5$ Å^{-1}, $N_{or} = 500$. N_{beams}^{min} and N_{beams}^{max} are the minimum and maximum number of beams that occurred in the structure matrix $\mathbf{A}$ during the N_{or} individual calculations.

Varied parameter	$wR2$ (%)	$R2$ (%)	$R1$ (%)	Thickness (Å)	U(Si) (Å^2)	N_{beams}^{min}	N_{beams}^{max}
Variable S_g^{max}							
0.010	5.83	4.76	2.95	113.22 (74)	0.0045 (9)	18	30
0.015	5.78	4.78	2.84	117.25 (84)	0.0031 (8)	29	40
0.020	5.81	4.33	2.74	116.10 (83)	0.0040 (8)	41	56
0.025	5.27	3.71	2.44	116.25 (83)	0.0039 (7)	53	71
0.030	5.11	3.64	2.40	116.32 (80)	0.0039 (7)	64	83
0.035	5.21	3.68	2.40	116.22 (80)	0.0042 (7)	80	99
0.040	5.20	3.67	2.44	116.35 (82)	0.0046 (7)	94	109
Variable g_{max}							
1.5	7.13	5.19	3.49	116.39 (103)	0.0073 (10)	33	39
2.0	5.35	3.82	2.57	116.23 (83)	0.0048 (7)	46	59
2.5	5.11	3.64	2.40	116.32 (80)	0.0039 (7)	64	83
3.0	5.15	3.66	2.43	116.51 (81)	0.0037 (7)	105	127
3.5	5.09	3.65	2.41	116.57 (78)	0.0036 (7)	137	159
4.0	5.09	3.66	2.42	116.62 (78)	0.0036 (7)	155	170

maxima. Despite these phenomena it can be concluded that $S_g^{max} = 0.03$ Å^{-1} is satisfactory for the silicon data sets and $S_g^{max} = 0.02$ Å^{-1} should be a good compromise between accuracy and speed for orthopyroxene.

The last question to be answered is, what is the influence of the parameter choice on the refined structure parameters, *i.e.* how does the choice of the parameters affect the accuracy of the refinement? To investigate this effect, we have selected five data sets: si2p1.0, si3p2.0, opht1p2.4, oplt2p2.4 and gito1p1.4, and performed structure refinements on these data sets with a series of g_{max} and S_g^{max} values. The details of the refinement are given below in the sections describing the refinements on individual samples. The results are summarized in Tables 2, 3, 4, 5, 6 and some of them are illustrated

graphically in Fig. 8. One can see that the choice of $g_{max} = 2.5$ Å^{-1} is perfectly fine for all test cases, and for all but si3p3.0, which is the thickest of all measured samples, 2.0 would also be a suitable choice. The selection of S_g^{max} is more complicated. For silicon $S_g^{max} = 0.025$ Å^{-1} seems a good choice. For the data set opht1p2.4 there is a clear minimum of the $wR2$ values for $S_g^{max} = 0.01$ Å^{-1}, which is then equaled only for $S_g^{max} = 0.03$ Å^{-1}. Its origin is unclear, but it corresponds to the similar minimum in Fig. 7. As this minimum is not reproduced in the $R2$ and $R1$ values, and it does not appear in the data set oplt2p2.4 (Table 5), we conclude that it probably results from a coincidentally good match with a few strong reflections. Neglecting this minimum, the R values decrease slowly but steadily up to $S_g^{max} = 0.03$ Å^{-1} for orthopyroxene and GITO. The variation of the refined parameters is at the level of up to 1.5 e.s.d.'s – but usually less – between $S_g^{max} = 0.02$ and 0.03 Å^{-1}. This suggests that a high value for S_g^{max} would be preferential, but a value as low as 0.02 Å^{-1} provides satisfactory results. To limit the computing time to manageable levels, we opted for $S_g^{max} = 0.02$ Å^{-1} and $g_{max} = 2.0$ Å^{-1} in the refinements of the orthopyroxene data sets. For the silicon data sets $S_g^{max} = 0.03$ Å^{-1} and $g_{max} = 2.5$ Å^{-1} were used.

Crucial for the successful refinement is the dependence of the minimized function on the orientation of the zone axis. As described in §3.1, the orientation cannot be reliably refined and must be determined by a grid search. Fig. 4 shows the dependence of $wR2$ as a function of the tilt of the zone axis from the exact position parallel to the incident beam for several silicon data sets. It shows clearly the decreasing sensitivity of the refinement on the exact orientation with increasing precession angle. A large precession angle thus permits one to find the correct orientation even if the initial guess of the orientation is off by more than 1°.

4.2. Silicon

The data sets from the silicon sample cover a wide range of precession angles and thicknesses. It was therefore possible to use these data sets to investigate systematically various parameters of the calculations and their impact on the figures of merit and refined parameters. The structure contains only one refinable parameter, the isotropic atomic displacement parameter U(Si). In addition to U(Si), the sample orientation, the thickness and the scale factor between calculated and experimental intensities were optimized.

We performed the refinement on all 16 data sets, that is four data sets with different precession angles from each of the four spots, with $S_g^{max} = 0.03$ Å^{-1} and $g_{max} = 2.5$ Å^{-1}. The results are summarized in Table 7. The table reveals a wealth of information on the behavior of the refinement from PED data. The values of $wR2$ and $R2$ decrease without exception when going from $\varphi = 1.0°$ to $\varphi = 3.0°$, and the same is valid with a single exception for $R1$. Interestingly, the $wR2$ and $R2$ values

Table 4
Results of test refinements on data set opht1p2.4 with various parameters of the Bloch-wave calculation.

Default parameter values: $S_g^{max} = 0.01$ Å^{-1}, $g_{max} = 2.0$ Å^{-1}, $N_{or} = 144$. N_{beams}^{min} and N_{beams}^{max} are the minimum and maximum number of beams that occurred in the structure matrix **A** during the N_{or} individual calculations.

Varied parameter	$wR2$ (%)	$R2$ (%)	$R1$ (%)	Thickness (Å)	occ(Fe1)	occ(Fe2)	N_{beams}^{min}	N_{beams}^{max}
Variable S_g^{max}								
0.0025	9.02	10.36	11.75	47.62 (49)	0.1415 (102)	0.4432 (30)	61	110
0.0050	8.18	9.34	10.67	48.52 (45)	0.1647 (96)	0.4276 (27)	142	197
0.0075	7.35	8.66	10.21	48.15 (43)	0.1840 (83)	0.4368 (25)	233	271
0.0100	7.00	8.47	9.90	49.09 (39)	0.1652 (80)	0.4403 (24)	325	339
0.0150	7.55	8.25	9.51	52.41 (50)	0.1716 (87)	0.4163 (26)	426	602
0.0200	7.46	8.08	8.77	51.17 (44)	0.1654 (88)	0.4333 (26)	565	844
0.0250	7.23	7.95	8.75	50.75 (43)	0.1750 (86)	0.4340 (25)	727	1062
0.0300	6.92	7.57	8.60	51.23 (44)	0.1771 (82)	0.4354 (24)	873	1213
Variable g_{max}								
1.50	7.07	8.70	9.98	49.20 (39)	0.1611 (81)	0.4351 (24)	234	248
2.00	7.00	8.47	9.90	49.09 (39)	0.1652 (80)	0.4403 (24)	325	339
2.50	7.03	8.52	9.96	49.10 (40)	0.1657 (81)	0.4405 (24)	430	446

Table 5
Results of test refinements on data set oplt2p2.4 with various parameters of the Bloch-wave calculation.

Default parameter values: $S_g^{max} = 0.01$ Å^{-1}, $g_{max} = 2.0$ Å^{-1}, $N_{or} = 144$. N_{beams}^{min} and N_{beams}^{max} are the minimum and maximum number of beams that occurred in the structure matrix **A** during the N_{or} individual calculations.

Varied parameter	$wR2$ (%)	$R2$ (%)	$R1$ (%)	Thickness (Å)	occ(Fe1)	occ(Fe2)	N_{beams}^{min}	N_{beams}^{max}
Variable S_g^{max}								
0.0025	8.23	11.14	15.17	39.02 (49)	0.0933 (103)	0.4910 (32)	61	116
0.0050	8.95	11.45	14.27	40.22 (52)	0.1100 (113)	0.4756 (34)	136	209
0.0075	8.04	10.65	13.69	39.21 (50)	0.1527 (103)	0.4962 (32)	210	308
0.0100	7.43	9.95	13.09	40.54 (47)	0.1355 (96)	0.4997 (30)	276	412
0.0150	7.17	9.52	13.02	42.14 (48)	0.1197 (95)	0.4740 (29)	400	680
0.0200	7.08	9.13	12.66	41.97 (46)	0.1071 (93)	0.4934 (29)	536	963
0.0250	6.90	8.93	12.65	42.13 (45)	0.1180 (92)	0.4970 (28)	676	1145
0.0300	6.79	8.90	12.64	42.01 (44)	0.1218 (91)	0.4914 (27)	813	1224
Variable g_{max}								
1.50	7.69	10.48	13.54	40.52 (48)	0.1264 (98)	0.4988 (31)	199	296
2.00	7.43	9.95	13.09	40.54 (47)	0.1355 (96)	0.4997 (30)	276	412
2.50	7.45	9.95	13.05	40.51 (47)	0.1363 (96)	0.5030 (30)	401	574

Table 6
Results of refinements on the data set gito2p1.4 with various parameters of the Bloch-wave calculation.

Default parameter values: $S_g^{max} = 0.02$ Å^{-1}, $g_{max} = 2.5$ Å^{-1}, $N_{or} = 100$. N_{beams}^{min} and N_{beams}^{max} are the minimum and maximum number of beams that occurred in the structure matrix **A** during the N_{or} individual calculations.

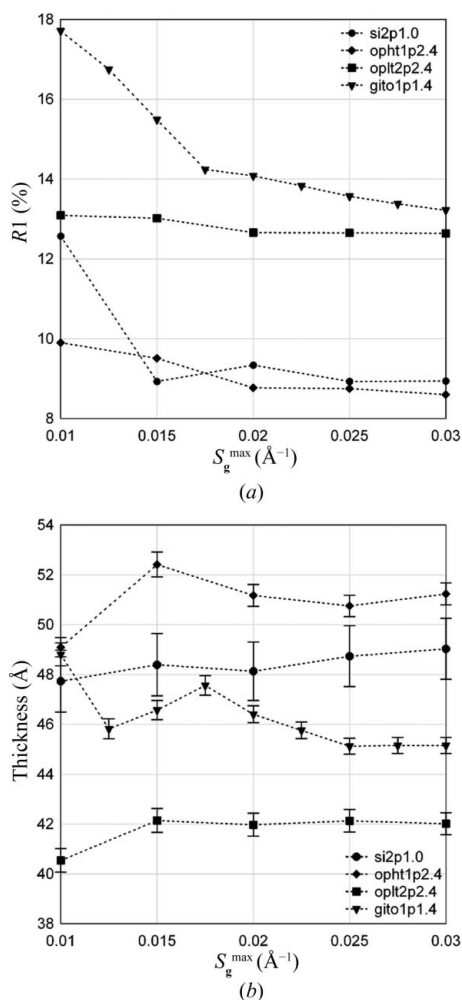| Varied parameter	$wR2$ (%)	$R2$ (%)	$R1$ (%)	Thickness (Å)	occ(In1)	occ(In2)	N_{beams}^{min}	N_{beams}^{max}
Variable S_g^{max}								
0.0100	31.30	28.04	17.71	48.80 (46)	0.489 (54)	0.802 (56)	452	626
0.0125	29.18	26.34	16.75	45.82 (40)	0.768 (51)	1.044 (57)	549	780
0.0150	28.42	25.25	15.49	46.57 (39)	0.497 (45)	0.877 (50)	644	910
0.0175	27.78	24.19	14.24	47.56 (39)	0.575 (46)	0.867 (42)	745	999
0.0200	27.07	23.67	14.08	46.40 (34)	0.564 (38)	0.844 (36)	793	1063
0.0225	26.70	23.26	13.83	45.76 (33)	0.559 (37)	0.848 (34)	871	1107
0.0250	26.63	22.91	13.57	45.12 (32)	0.486 (44)	0.754 (40)	969	1153
0.0275	26.55	22.80	13.38	45.15 (32)	0.534 (39)	0.838 (31)	1025	1200
0.0300	26.58	22.69	13.22	44.94 (32)	0.518 (41)	0.828 (32)	1105	1244
Variable g_{max}								
1.50	28.21	24.06	15.19	41.74 (32)	0.675 (44)	0.874 (46)	483	606
1.75	27.27	23.89	14.91	45.11 (37)	0.434 (41)	0.781 (40)	619	708
2.00	27.51	24.40	15.49	43.66 (35)	0.455 (42)	0.846 (41)	757	815
2.25	27.24	23.66	14.23	45.46 (36)	0.478 (42)	0.854 (38)	801	943
2.50	27.07	23.67	14.08	46.40 (34)	0.564 (38)	0.844 (36)	793	1063

Figure 8
Refinement results on selected data sets with varying S_g^{max}. (a) Refinement R value $R1$, (b) refined thickness. Dotted lines are guides for eye.

Table 7
Refinement results from the silicon data sets – dynamical refinement.

Data set	$wR2$ (%)	$R2$ (%)	$R1$ (%)	Thickness (Å)	U(Si) (Å^2)
si1p0.0	16.22	12.40	15.77	41.45 (63)	0.0143 (23)
si1p1.0	12.77	10.80	7.10	36.73 (66)	0.0106 (14)
si1p2.0	7.18	6.00	3.66	39.90 (66)	0.0090 (11)
si1p3.0	6.98	5.88	4.63	35.22 (78)	0.0039 (14)
si2p0.0	8.35	6.63	12.98	38.20 (29)	0.0026 (09)
si2p1.0	14.64	10.10	8.94	49.06 (123)	0.0171 (26)
si2p2.0	8.54	6.92	3.60	41.27 (68)	0.0069 (11)
si2p3.0	5.40	4.39	2.72	39.51 (55)	0.0048 (9)
si3p0.0	11.65	8.88	18.82	104.88 (24)	0.0053 (3)
si3p1.0	17.97	12.70	9.04	107.30 (159)	0.0054 (19)
si3p2.0	8.17	6.55	4.31	113.18 (88)	0.0054 (10)
si3p3.0	5.07	3.82	2.52	116.55 (82)	0.0033 (7)
si4p0.0	23.37	23.46	21.99	83.66 (44)	0.0068 (7)
si4p1.0	16.33	11.56	7.77	104.89 (136)	0.0007 (13)
si4p2.0	11.81	8.73	5.81	83.26 (103)	0.0068 (14)
si4p3.0	8.04	7.15	3.66	83.96 (52)	0.0027 (12)

Table 8
Refinement results from the silicon data sets – kinematical refinement.

Data set	$wR2$ (%)	$R2$ (%)	$R1$ (%)	U(Si) (Å^2)
si1p0.0	68.42	64.74	49.10	0.1145 (418)
si1p1.0	55.22	43.34	40.25	0.0070 (72)
si1p2.0	43.44	27.52	28.99	−0.0037 (45)
si1p3.0	39.14	25.53	27.58	0.0061 (49)
si2p0.0	34.92	33.76	32.93	0.0836 (128)
si2p1.0	56.24	41.48	38.30	−0.0008 (60)
si2p2.0	45.38	32.00	30.80	−0.0049 (44)
si2p3.0	40.13	25.80	27.31	0.0048 (46)
si3p0.0	38.63	38.14	36.51	0.0926 (173)
si3p1.0	60.76	53.75	44.94	−0.0097 (58)
si3p2.0	49.35	36.63	31.54	−0.0131 (45)
si3p3.0	39.97	28.13	28.16	−0.0094 (36)
si4p0.0	36.53	36.66	51.14	0.2049 (319)
si4p1.0	63.65	56.37	46.17	−0.0099 (61)
si4p2.0	50.93	35.49	30.78	−0.0143 (45)
si4p3.0	48.62	38.26	33.16	−0.0107 (44)

Table 9
Refinement results from the silicon data sets – two-beam refinement.

Data set	$wR2$ (%)	$R2$ (%)	$R1$ (%)	Thickness (Å)	U(Si) (Å^2)
si1p0.0	37.24	33.48	40.64	35.20 (66)	0.0170 (155)
si1p1.0	51.06	37.77	33.78	29.82 (670)	−0.0043 (119)
si1p2.0	43.21	28.18	28.81	37.64 (489)	−0.0032 (78)
si1p3.0	38.75	24.59	26.52	40.84 (408)	0.0114 (90)
si2p0.0	36.74	36.49	45.11	45.95 (41)	0.0444 (97)
si2p1.0	52.96	39.34	37.43	34.41 (1145)	−0.0026 (161)
si2p2.0	44.77	31.54	30.34	39.52 (515)	−0.0027 (76)
si2p3.0	39.41	24.43	26.01	41.17 (393)	0.0086 (78)
si3p0.0	21.77	21.75	31.26	117.41 (62)	−0.0284 (52)
si3p1.0	40.30	28.58	26.70	122.17 (831)	−0.0189 (59)
si3p2.0	46.88	31.44	29.18	100.49 (660)	0.0004 (70)
si3p3.0	37.97	24.19	25.29	121.76 (1048)	0.0120 (66)
si4p0.0	26.91	26.21	34.71	84.50 (45)	−0.0650 (54)
si4p1.0	42.57	27.54	25.65	68.99 (336)	−0.0410 (50)
si4p2.0	48.98	34.36	29.83	72.63 (428)	0.0014 (59)
si4p3.0	45.94	33.63	29.32	83.37 (669)	−0.0016 (55)

of the data sets without precession are high in three cases, but relatively low in one case. In no case are they lower than the corresponding data set with $\varphi = 3.0°$. The thickness refines in general to similar values for individual spots, but there are exceptions. It is difficult to judge the correctness of the thickness because we do not have an independent estimation of this parameter, but from the table it seems that the most significant outliers are data sets si2p1.0 and si4p1.0. The values of U(Si) are positive in all cases, but unrealistically high for data sets si1p0.0 and si2p1.0, and clearly too low for the data set si4p1.0. For other data sets the values are not unrealistic, although some of them deviate significantly from the expected literature value of 0.007 Å^2 (Yim & Paff, 1974). There seems to be a systematic trend towards lower U(Si) from data sets with increasing precession angles.

Tables 8 and 9 show the results of the kinematical and two-beam refinements. The kinematical refinement results in very large R values and often unrealistic values of U(Si). The R values tend to decrease with increasing precession angle, confirming the general rule that with increasing precession angle the diffracted intensities become closer to the kinema-

tical intensities. Nevertheless, even for a high precession angle the match is poor and the refined U(Si) unrealistic. Interestingly, the R values for data sets without precession can be lower than for some data sets with precession. This is because
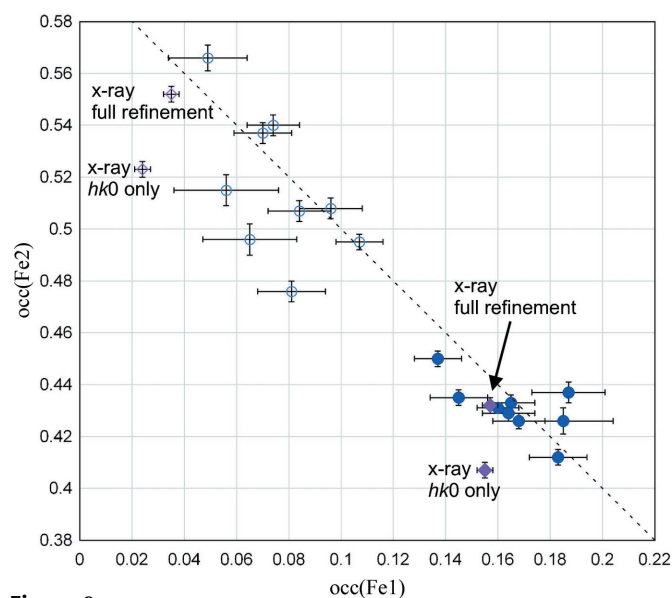
Table 10
Refinement of the data sets from the treated orthopyroxene sample, dynamical refinement.

Data set	wR2 (%)	R2 (%)	R1 (%)	Thickness (Å)	occ(Fe1)	occ(Fe2)
opht1p1.6	7.57	8.61	8.74	52.34 (34)	0.1450 (110)	0.4347 (29)
opht2p1.6	9.54	9.71	8.43	45.17 (37)	0.1870 (137)	0.4375 (36)
opht3p1.6	13.55	13.64	10.23	50.83 (49)	0.1846 (188)	0.4258 (51)
opht1p2.4	7.46	8.08	8.77	51.17 (44)	0.1654 (88)	0.4333 (26)
opht2p2.4	9.04	9.05	9.60	46.11 (46)	0.1638 (102)	0.4286 (31)
opht3p2.4	9.97	9.82	9.31	55.41 (48)	0.1832 (107)	0.4121 (31)
opht1p2.8	7.15	7.98	10.19	51.27 (37)	0.1597 (83)	0.4310 (24)
opht2p2.8	8.77	8.67	9.91	44.91 (51)	0.1366 (93)	0.4498 (30)
opht3p2.8	9.36	9.38	10.10	52.03 (45)	0.1677 (100)	0.4261 (30)
XRD, all data	6.58	5.97	3.43		0.1567 (32)	0.4321 (31)
XRD, hk0 only	9.01	6.36	4.08		0.1597 (37)	0.4083 (33)

Table 11
Refinement of the data sets from the treated orthopyroxene sample, kinematical refinement.

Data set	wR2 (%)	R2 (%)	R1 (%)	occ(Fe1)	occ(Fe2)
opht1p1.6	38.84	42.79	37.63	−0.1244 (497)	0.4445 (208)
opht2p1.6	39.55	40.98	35.43	−0.0725 (458)	0.3611 (190)
opht3p1.6	41.89	41.05	36.33	−0.0617 (499)	0.3988 (211)
opht1p2.4	36.80	43.23	36.34	−0.1439 (432)	0.2038 (168)
opht2p2.4	35.67	39.82	34.01	−0.0904 (391)	0.2316 (157)
opht3p2.4	38.58	40.36	34.07	−0.1442 (418)	0.2313 (171)
opht1p2.8	35.95	42.18	35.28	−0.1324 (431)	0.2111 (167)
opht2p2.8	34.97	39.69	32.92	−0.0842 (392)	0.2531 (159)
opht3p2.8	37.20	39.81	32.92	−0.0968 (412)	0.2425 (169)

the high-resolution reflections are very weak in the non-precessed data. Refining the U to a high value makes the calculated intensities also very low and ensures a comparably good match to the experimental intensities.

The two-beam refinement yields generally better R values than the kinematical refinement. The difference is most important for low precession angles and it decreases – but does not vanish – for high precession angles. The refined U(Si) vary much more than in the dynamical refinement, and they can be negative, but they are closer to the correct values than the kinematical refinement, with a notable exception of $\varphi = 1.0°$. The refined values of the thickness also vary much more than in the dynamical refinement, but especially for the two largest precession angles they still represent a good guess of the correct values, with the deviation from the corresponding dynamical refinement under 15%.

4.3. Orthopyroxene

The structure of orthopyroxene contains ten independent atomic positions, two of which exhibit a mixed Fe/Mg occupancy. It would be unfeasible to perform full structure refinement on all 18 available data sets. Therefore we refined only the thickness and the two occupancy factors, and kept all other structural parameters at their values obtained from the refinement against X-ray diffraction data. Finally, for one selected data set we performed a full structure refinement, excluding only parameters that are not refinable from the 001 zone-axis data.

All 18 data sets were refined with the parameters $S_{\mathbf{g}}^{max} = 0.02$ Å^{-1} and $g_{max} = 2.0$ Å^{-1} (Tables 10 and 13, Fig. 9). For the heat-treated sample, the occupancies refined from different data sets agree mutually very well, with the maximum difference of 5% for occ(Fe1) and 2.5% for occ(Fe2). The refinement R values are in general at or below

Figure 9
Refined occupancies of Fe1 and Fe2 in the natural (empty symbols) and heat-treated (full symbols) orthopyroxene samples. Diamonds represent the refinement against the complete X-ray data set and against the hk0 reflections from the X-ray data set.
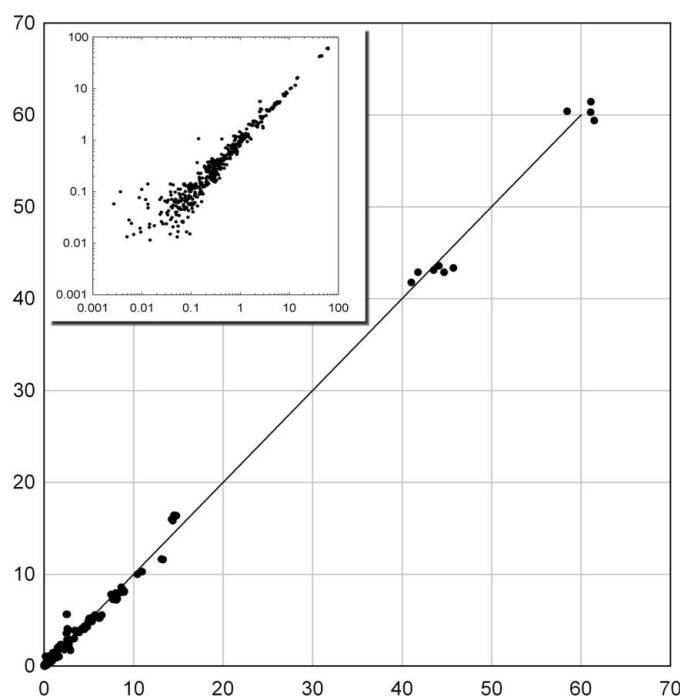

Figure 10
I° versus I^{c} plot of the data set opht1p2.4. The inset shows the same plot on a logarithmic scale.

Table 12
Refinement of the data sets from the treated orthopyroxene sample, two-beam refinement.

Data set	wR2 (%)	R2 (%)	R1 (%)	Thickness (Å)	occ(Fe1)	occ(Fe2)
opht1p1.6	25.83	29.82	32.02	57.08 (138)	0.4941 (286)	0.5894 (94)
opht2p1.6	27.61	26.66	29.61	57.83 (156)	0.4295 (288)	0.4958 (92)
opht3p1.6	31.15	29.34	30.83	63.61 (170)	0.4689 (317)	0.4778 (102)
opht1p2.4	23.30	24.43	30.00	45.77 (190)	0.3037 (311)	0.4352 (90)
opht2p2.4	24.12	22.99	27.86	41.21 (188)	0.2439 (308)	0.3999 (89)
opht3p2.4	27.98	25.53	28.91	52.65 (182)	0.2511 (338)	0.3909 (98)
opht1p2.8	21.85	23.77	29.80	43.66 (164)	0.2493 (310)	0.3910 (86)
opht2p2.8	22.68	22.08	26.85	36.34 (230)	0.2120 (305)	0.3909 (87)
opht3p2.8	25.59	23.78	27.95	48.64 (170)	0.2407 (319)	0.3763 (91)

Table 13
Refinement of the data sets from the natural orthopyroxene sample, dynamical refinement.

Data set	wR2 (%)	R2 (%)	R1 (%)	Thickness (Å)	occ(Fe1)	occ(Fe2)
oplt1Ap2.4	13.18	13.42	14.25	46.13 (71)	0.0490 (150)	0.5662 (53)
oplt1Bp2.4	8.29	10.29	14.24	42.03 (62)	0.0955 (115)	0.5084 (35)
oplt2p2.4	7.07	9.13	12.66	41.99 (46)	0.1074 (93)	0.4946 (29)
oplt3p2.4	13.71	16.85	18.56	33.47 (85)	0.0557 (204)	0.5154 (63)
oplt1Ap2.8	9.54	10.25	14.57	44.82 (53)	0.0743 (104)	0.5400 (36)
oplt1Bp2.8	9.20	11.13	16.11	42.61 (56)	0.0705 (107)	0.5373 (37)
oplt1Cp2.8	14.15	15.59	15.05	43.57 (92)	0.0651 (179)	0.4955 (56)
oplt2p2.8	10.14	13.16	16.89	43.15 (75)	0.0811 (131)	0.4760 (39)
oplt3p2.8	9.20	11.36	14.39	44.32 (64)	0.0844 (118)	0.5067 (37)
XRD, all data	6.56	5.32	3.15		0.0352 (34)	0.5517 (33)
XRD, hk0 only	7.64	4.30	3.31		0.0285 (30)	0.5243 (29)

Table 14
Refinement of the data sets from the natural orthopyroxene sample, kinematical refinement.

Data set	wR2 (%)	R2 (%)	R1 (%)	occ(Fe1)	occ(Fe2)
oplt1Ap2.4	38.31	44.88	36.60	−0.1863 (427)	0.3422 (182)
oplt1Bp2.4	28.76	38.71	36.94	−0.1753 (352)	0.3368 (139)
oplt2p2.4	32.99	42.27	38.17	−0.1607 (399)	0.2661 (154)
oplt3p2.4	30.36	36.76	34.50	−0.1443 (362)	0.3663 (146)
oplt1Ap2.8	38.44	47.18	37.50	−0.1417 (437)	0.3026 (184)
oplt1Bp2.8	35.78	45.70	39.37	−0.1473 (429)	0.3048 (175)
oplt1Cp2.8	31.77	37.50	34.37	−0.1569 (365)	0.3557 (149)
oplt2p2.8	34.11	42.68	38.82	−0.1647 (413)	0.2995 (162)
oplt3p2.8	29.64	38.41	35.82	−0.1491 (357)	0.3439 (142)

Table 15
Refinement of the data sets from the natural orthopyroxene sample, two-beam refinement.

Data set	wR2 (%)	R2 (%)	R1 (%)	Thickness (Å)	occ(Fe1)	occ(Fe2)
oplt1Ap2.4	27.34	30.12	31.60	45.38 (242)	0.1680 (370)	0.5036 (112)
oplt1Bp2.4	18.34	23.71	30.56	29.24 (210)	0.2309 (283)	0.5370 (83)
oplt2p2.4	17.83	21.91	29.66	31.63 (210)	0.2777 (263)	0.5214 (78)
oplt3p2.4	21.73	26.07	29.83	33.01 (207)	0.2227 (321)	0.4960 (94)
oplt1Ap2.8	25.56	28.67	30.77	33.06 (360)	0.1497 (361)	0.4596 (108)
oplt1Bp2.8	21.90	26.84	31.56	32.15 (211)	0.1598 (330)	0.4615 (97)
oplt1Cp2.8	22.95	25.48	28.96	31.79 (250)	0.2004 (329)	0.4982 (95)
oplt2p2.8	18.33	22.70	29.65	31.82 (155)	0.2026 (277)	0.4706 (78)
oplt3p2.8	19.06	22.81	28.76	31.85 (186)	0.2168 (290)	0.5098 (82)

10%, with a single exception of the data set opht3p1.6. No significant trend can be observed with increasing precession angle. The refined occupancies agree very well also with the reference refinement against X-ray diffraction data.

The results are somewhat less consistent for the natural sample. The R values are more elevated, with wR2 ranging from 7.07 to 14.15%, and R1 typically around 15%. Also the spread of the refined occupancies is larger, being 5.8% for occ(Fe1) and 9% for occ(Fe2). There is also a discrepancy of a few percent between the refined values and the reference X-ray structure. As the experimental conditions, the data treatment and the refinement procedure were exactly the same for both samples, the difference has to come from the sample itself. The sample has not been thermally treated, and might exhibit local inhomogeneities and defects, leading to both the elevated R values and the spread of the occupancies.

All data sets share one particular feature – the R2 values are very similar to R1, and often they are slightly lower than R1. This is unusual. It follows from the definition of the R values that, statistically, R2 should be roughly two times larger than R1. This is approximately fulfilled for most of the silicon data sets (Table 7) and also for the data set gito1p1.4 (Table 6). However, the analysis of the distribution of I^o versus I^c in the orthopyroxene data sets did not reveal any systematic bias (Fig. 10). It seems that this unusual behavior is caused by the special distribution of the intensities, where ten reflections

(three symmetry independent) dominate the distribution. A good fit to these ten reflections then dominates R2 much more than R1. As an example, when the ten strongest reflections are excluded, the R2 and R1 values for the data set opht1p2.4 rise from 8.25 to 13.59% and from 8.91 to 10.39%, respectively.

Tables 11 and 12, and 14 and 15 report the refinements with the kinematical and two-beam model, respectively. Similarly to silicon, the kinematical refinement results in rather poor R values and wrong refined parameters – occ(Fe1) consistently refines to negative values for all data sets. The two-beam refinement brings a significant improvement of both the R values and the parameters. The R2 values drop by 10–20%, R1 drop by 5–9%. Even more importantly, the thickness refines to values close to the correct values, and the occupancies also refine to much better values compared with the kinematical refinement, although occ(Fe1) refines consistently to a too high number.

For both samples X-ray diffraction data from the bulk sample were available (for details see Jacob et al., 2013). Tables 10 and 13 and Fig. 9 also contain the refined occupancies from these data for reference. In addition to the complete standard X-ray refinement we performed a refinement analogous to the refinement from electron diffraction data, with only hk0 reflections, with all parameters fixed except for the two occupancies, with isotropic displacement parameters and with a non-averaged reflection set. Maybe surprisingly, the occupancies from the two X-ray refinements show a relatively large spread. The spread is comparable to the spread of the values from electron diffraction, although the

Table 16
Refinement of all permitted structure parameters of the orthopyroxene structure against the data set opht1p2.4.

Maximum and average distance mean the distances from the reference structure refined against X-ray diffraction data.

	Kinematical	Two-beam	Dynamical
$wR2$, $R2$, $R1$ (%)	15.80, 20.63, 30.61	15.69, 19.49, 28.54	5.45, 7.48, 11.25
Maximum U_{iso} (Å^2)	0.0886	0.1794	0.0581
Minimum U_{iso} (Å^2)	−0.0099	−0.0164	−0.0085
Maximum distance (Å)	0.302	0.146	0.093
Total average distance (Å)	0.122	0.106	0.048
Average distance of cations (Å)	0.044	0.108	0.050
Average distance of O atoms (Å)	0.175	0.105	0.047
occ(Fe1)	0.571	0.413	0.134
occ(Fe2)	1.094	1.278	0.436

two X-ray refinements used the same data set, while the electron data come from different experiments.

Data set opht1p2.4 was also used for a full structure refinement, where all x and y coordinates of all atoms were optimized as well as their U_{iso} values and occupancies of the mixed sites. The z coordinates were fixed to the values obtained from the X-ray refinement. Such a model contains 34 refinable parameters. First a kinematical refinement was performed. It converged to the $wR2$ value of 15.80%, but the occupancy of the atoms Fe2/Mg2 refined to unphysical values (Table 16) and two out of ten displacement parameters refined to a negative value. The maximum distance of the refined atomic positions from the reference X-ray refinement was 0.302 Å, the average distance was 0.122 Å. We note that errors of this magnitude are typical for kinematical refinements. Then, starting from the result of the kinematical refinement, a two-beam refinement was performed. It converged to $wR2 =$ 15.69%, and the occupancy of Fe2/Mg2 refined to even more unphysical values due to the strong correlation with the isotropic displacement parameter. Five atoms had negative displacement parameters. However, the maximum distance of an atom from the positions in the reference X-ray structure decreased to 0.146 Å and the average distance to 0.106 Å. Finally, the result of the two-beam refinement was used as a starting point for a full dynamical refinement. It turned out that the displacement parameters and occupancies were so far from the correct values that they prevented the convergence of the refinement to the correct minimum. Therefore the occupancies were reset to 0.5 and all U_{iso} were set to 0.01. The coordinates were retained from the two-beam refinement. This refinement converged smoothly to $wR2 = 5.45\%$. The occupancies were close to the expected values. Four displacement parameters refined to negative values, but only one differed from zero by more than two e.s.d.'s. The maximum distance of an atom from the X-ray result was 0.093 Å, the average distance was 0.048 Å. The three refinements are compared in more detail in Table 16. It should be emphasized that the full refinement against only one zone axis is presented here only for illustration. It cannot be taken seriously, as the amount of data is not sufficient for a robust refinement of all parameters. The refinement converges to very similar values if started from the X-ray structure, and the differences are thus

not due to the inability of the algorithm to find the correct minimum.

4.4. Gallium–indium tin oxide

The structure of GITO contains 17 independent atomic positions, two of which have mixed occupancy. We had only one precession data set for this sample and thus the test calculations (Table 6) are at the same time the final results. In these refinements only the thickness and the occupancies were refined, and all other structural parameters were kept fixed. Most parameters were fixed to the values from the neutron powder diffraction refinement (Edwards *et al.*, 2000). However, the displacement parameters of Ga1, Ga2, In1, In2, Sn1 and Sn2 were obviously inconsistent, and they were therefore reset to a mean value of 0.006 Å^2. The results in Table 6 are within three e.s.d.'s of the published values occ(In1) = 0.48 (4) and occ(In2) = 0.72 (4).

The kinematical refinement resulted in very poor R values ($wR2 = 61.47$, $R2 = 59.32$, $R1 = 47.77\%$) and physically meaningless occupancies [occ(In1) = −3.59 (14), occ(In2) = 1.79 (18)]. In agreement with the other samples, the two-beam refinement resulted in better R values ($wR2 = 53.56$, $R2 = 52.48$, $R1 = 44.65\%$) and improved refined parameters [occ(In1) = −0.47 (9), occ(In2) = 0.69 (9)]. Nevertheless, these R values are still very high and one of the refined occupancies is very far from the correct value. Finally, the refinement of the data collected without precession also resulted in very poor R values ($wR2 = 55.31$, $R2 = 55.76$, $R1 = 43.86\%$).

A full dynamical refinement of all structure parameters was also attempted with the same data set. Because all atoms sit on positions with a fixed value of the y coordinate, a complete structure refinement is in principle possible against one zone only. The refinement was performed with $S_g^{max} = 0.02$ Å^{-1} and $g_{max} = 2.0$ Å^{-1}. The principal results of the refinement are summarized in Table 17. It is visible from the table that the refinement is not satisfactory, with atomic shifts up to 0.44 Å from the reference structure. The occupancies of In1/In2 also differ from the reference values, although they refine to physically meaningful values. However, an inspection of the two-beam and kinematical refinement shows that the latter two are completely unstable, with atomic shifts exceeding 1 or even 2 Å, with unphysical displacement parameters and occupancies. Compared to the kinematical and two-beam refinements, the full dynamical refinement yields much better agreement with the reference structure (Edwards *et al.*, 2000).

5. Discussion

The analysis of the three samples allows us to make several general statements. To state first the obvious, our results show that the precession electron diffraction data are suitable for accurate structure refinement, unlike the refinement using the

Table 17
Refinement of all parameters of the structure GITO against the data set gito1p1.4.

Maximum and average distance mean the distances from the reference structure refined against neutron diffraction data.

	Kinematical	Two-beam	Dynamical
$wR2$, $R2$, $R1$ (%)	34.61, 29.38, 21.93	30.60, 27.01, 20.27	21.42, 17.84, 11.55
Maximum U_{iso} (Å^2)	0.2980	0.3685	0.0507
Minimum U_{iso} (Å^2)	−0.0340	−0.0367	−0.0241
Maximum distance (Å)	2.748	1.299	0.449
Total average distance (Å)	1.043	0.536	0.164
Average distance of cations (Å)	0.665	0.216	0.077
Average distance of O atoms (Å)	1.232	0.696	0.207
occ(In1)	−2.071 (82)	2.952 (162)	0.283 (46)
occ(In2)	−0.193 (137)	1.752 (88)	0.984 (46)

kinematical or two-beam approximation, which should be considered as first, preliminary steps towards the full dynamical refinement. Our results also show that for moderate or large thicknesses the refinement against diffraction data collected without precession is clearly inferior to the refinement with precession. The difference is obvious already in the silicon data, which come from a very simple structure and a perfect crystal, and it becomes critical in the other two data sets coming from less perfect and more complex crystals, for which out of three data sets collected without precession only one (non-treated orthopyroxene data) yielded a reasonable match, the other two resulting in very poor refinement. The difference can be explained by the much lower sensitivity of the precessed intensities to the variation of thickness and orientation. Thus, a slightly bent or inhomogeneously thick crystal will yield a poor match with non-precessed data, while the match will still be acceptable for the precessed data. For the precessed data sets the results indicate that larger precession angles provide better fits and better quality of the refinement. This trend is especially clear in the silicon data, while it is less obvious in the orthopyroxene data. For the GITO sample we had only one data set with $\varphi = 1.375°$ and thus no conclusions can be made. Nevertheless, the low precession angle might be one of the reasons for the relatively high R values compared with the other samples.

The use of larger precession angles also has other advantages than the lower R values. It has often been stated that precession provides a reduced sensitivity to crystal misorientation from the zone-axis position. However, little or no quantitative analyses of this phenomenon have been presented. Here this question is approached quantitatively. As Fig. 4 clearly shows, the sensitivity of the fit to the variation of the orientation is strongly reduced with increasing precession angle. The same is true for the thickness. This allows for a smooth refinement even from relatively inaccurate starting parameters. In contrast, small precession angles (especially 0°, but also 1° to a certain extent) result in a much more complicated refinement landscape, and inaccurate choice of the starting parameters may lead to false minima in the refinement. Another advantage of higher precession angles is lower correlations between the refined parameters. This again is most obvious in the comprehensive silicon data set, where refinements with $\varphi = 0°$ and $\varphi = 1°$ resulted in large correlation coefficients between U(Si) and the thickness, reaching over 0.9 in some cases, while the same correlation coefficient stayed well below 0.5 for $\varphi = 2°$ and $\varphi = 3°$.

Analysis of four samples of three different structures permits us also to suggest some general rules for the best parameters of the Bloch-wave calculation. The selection of the beams to be included in the structure matrix is driven by g^{max} and S_g^{max}. In all our data sets the choice $g^{max} = 2.5$ Å^{-1} ensured a good match and even $g^{max} = 2.0$ Å^{-1} was sufficient in most cases. The choice of S_g^{max} is more difficult. For orthopyroxene and GITO it seems that going to higher S_g^{max} values than those listed in Tables 4, 5 and 6 might yield even better results. However, the computational complexity grows almost as the third power of S_g^{max}, and thus the calculations quickly become extremely time consuming. Obviously, one should use as high a value for S_g^{max} as possible, given the available time and computing power. However, $S_g^{max} = 0.02$ Å^{-1} yielded results very similar to the results obtained with higher S_g^{max}, and this value can be considered a good compromise between the accuracy and speed of calculations.

The choice of N_{or} does not depend too much on the particular structure, but it does depend on both the thickness and the value of φ. Inspection of Fig. 5 shows that, at least in the particular case of the silicon data sets, the dependence on both parameters is very roughly linear.

Comparing the standard deviations of the refined parameters with the refinement against X-ray data for the orthopyroxene sample and neutron data for the GITO sample, we see that the orthopyroxene refinement yields about three to five times larger e.s.d.'s for occ(Fe1) compared to the equivalent X-ray refinement, and very similar e.s.d.'s for the occ(Fe2). Interestingly, the refinement of only the $hk0$ reflections from the X-ray data sets yields occupancies that differ up to 8.7 e.s.d.'s from the reference values refined against all data. This confirms the well known fact that even high-quality X-ray data are not void of systematic bias and that the e.s.d.'s should be taken only as an indication of the true error rather than an absolute measure. A similar effect was observed by Merli *et al.* (2002), who used leverage analysis to study the effect of selectively removing certain classes of reflections on the structure refinement of pyroxenes. For GITO, the e.s.d.'s of the occupancies obtained from the electron diffraction data are close to the refinement from neutron powder data. It can be concluded that in our tests the refinement of occupancies against PED data yielded results that can bear comparison with the refinement against X-ray or neutron diffraction data.

The full structure refinements performed on one orthopyroxene data set and on the GITO data set show that such refinement is possible, and that the dynamical refinement yields positions with an accuracy superior to the accuracy of

the kinematical or two-beam refinement, especially for light atoms. Nevertheless, the full refinement of the GITO structure is not satisfactory, despite its considerable improvement over the kinematical and two-beam refinement. We see several possible explanations for this result. First, the data were collected on a sample crushed to a fine powder, and it is thus possible that the crystal was not homogeneously thick across the illuminated area. Second, the precession angle was only $1.375°$. The results on silicon show that low precession angles give worse results than higher angles. And third, it might be necessary to include absorption effects in this structure containing heavy atoms.

The data sets analyzed in this work were obtained by both selected-area electron diffraction (SAED) and with small-spot illumination. If SAED is used, reflections at higher diffraction angles come from other places on the sample than low-angle reflections, due to the spherical aberration of the objective lens. For quantitative work, it is therefore strongly recommended to use small-spot illumination, where this problem does not occur. Surprisingly, in our analysis, there is no obvious difference between the two illumination modes, in either of the two samples. A possible explanation is that both the silicon and orthopyroxene samples were large flat samples, and the fact that different reflections come from different places on the sample does not play an important role.

The aim of this work is to demonstrate the feasibility of the approach and to lay foundations for further development of the method. To keep the workload manageable, some aspects had to be neglected. One important aspect is the neglect of possible thickness variation in the illuminated sample. Both in the wedged sample of silicon and in the cleaved grain of GITO this variation may be non-negligible, and it should be included in a full analysis. Probably the most important simplification is the omission of absorption. To estimate its importance, we have calculated two simulated data sets using the multislice method implemented in the program *Numis* (Marks *et al.*, 1993), one for orthopyroxene and one for GITO. In each case, one simulation was performed without absorption and another with absorption effects included, assuming $U'/U = 0.05$. The $R2$ value between the two data sets was $R2 = 1.47\%$ for orthopyroxene and $R2 = 6.00\%$ for GITO. In light of the discussion in §4.1, it can be expected that the impact of the absorption will be negligible for the light-atom structures of silicon and orthopyroxene, and probably small, but observable, for GITO. Nevertheless, it is clearly preferable to include the absorption effects in the calculations to avoid any systematic bias that might be introduced if absorption is omitted.

Other possible effects that might influence the quality of the fit is the experimental setup, notably the quality of the alignment of the precession device, beam convergence and the inclusion of the inelastic scattering. The precession device is aligned before every experiment and care should be taken especially to align the beam pivot point, *i.e.* to ensure the vertex of the precessing cone is exactly on the sample, and the circularity of the precession circuit. In our experience, if care is taken, the circularity of the precession circuit can be aligned

very well, with deviations from perfect circularity being less than 1% of the used precession angle. The beam convergence is very small for the SAED data (<0.3 mrad) and probably does not play an important role for the fit. For microdiffraction data, the convergence angle can be non-negligible (up to 1.7 mrad in some of the orthopyroxene data) and the convergence might need to be taken into account in the refinement. However, in our tests, there was no significant difference between results obtained with SAED and microdiffraction data, indicating that even the beam convergence is not a very important factor, if not too large. The effect of inelastic scattering was not studied, as all the data sets were collected without energy filtering. It can be expected that inclusion of inelastic scattering will have an observable effect on the quality of the fit, although the effect will probably be small, at least for thin samples (Jansen *et al.*, 2004).

6. Conclusions and outlook

We have demonstrated on three materials that precession electron diffraction data can be successfully used for accurate determination of structural parameters. The three refined structures range from a simple structure of silicon to the more complex structures of orthopyroxene (ten independent atoms, $V_{UC} = 843$ Å^3) and gallium–indium tin oxide (17 independent atoms, $V_{UC} = 392$ Å^3). The thickness of the samples varies from *circa* 30 to 110 nm. The accuracy of the refined parameters can bear comparison with the structure refinement against X-ray or neutron diffraction data if the data-to-parameter ratio is not too low. We demonstrated that the precession diffraction data are superior to diffraction data collected without precession at least in four aspects: significantly lower figures of merit, higher accuracy of the refined parameters, much broader radii of convergence, especially for thickness and orientation of the sample, and significantly reduced correlations between the parameters.

We did not put any effort into optimizing the speed of calculations. This issue will be crucial for the routine application of the method. There are several possibilities for improving the speed. The most important is the replacement of the numerical derivatives with analytical formulae. Further possibilities include exploiting the 'Brillouin-zone folding' method (Sinkler & Marks, 2010), and the use of parallel computing, GPU programming and algorithms for operations with sparse matrices. We believe that by combining these methods we will shorten the computing time to the extent that a complete refinement of a moderately large structure will be possible within hours.

In future we want to focus on all aspects neglected in this work, with the primary focus on the speed of the calculations. An implementation of the refinement against PED data in the crystallographic computing system *Jana2006* (Petříček *et al.*, 2006) is currently in progress. Once finished, the crystallographic community will have at hand a tool for refinement from electron diffraction data with all the wealth of features that have been developed over the decades for X-ray and neutron structure refinements.

APPENDIX A
Integration of reflection intensities and estimation of their estimated standard deviations

A full and correct determination of net integrated intensities and their estimated standard deviations $\sigma(I)$ from a recorded diffraction pattern is a complicated issue. Already the CCD detector commonly used to record intensities introduces a number of effects that are non-trivial to quantify (Leslie, 1999; Phillips *et al.*, 2000; Waterman & Evans, 2010). The integrated intensities and their e.s.d.'s also depend on the integration scheme, peak shape and background model. However, in our case (and in most cases of well aligned electron diffraction patterns from good-quality crystals) the peak shape is well behaved, it does not change too much from reflection to reflection, and the background is smooth, without sharp features (Fig. 3). In such a case, a good estimation of the integrated intensities and a reasonable approximation to their $\sigma(I)$'s may be obtained with a simplified method. The method we adopted relies on the approximation that the $\sigma(p)$ of the counts p on each pixel has two main contributions: the diffraction signal itself, which is assumed to have a Poisson distribution, and the added noise from the detector. The latter, as it is a combination of many independent effects, can be assumed to have a Gaussian distribution. The counts p in each pixel thus have a variance given by the sum of the variance of the detector noise $\sigma_d^2(p)$ and of the diffraction signal $\sigma_s^2(p)$:

$$\sigma^2(p) = \sigma_d^2(p) + \sigma_s^2(p). \qquad (12)$$

The detector also contributes to the signal itself (dark current or bias), but this contribution is subtracted during the data processing, and the mean contribution to p from the detector after the dark-current subtraction is zero. Thus, we have $\langle p \rangle = \langle p_s \rangle$. Assuming a Poisson distribution, $\sigma_s^2(p) = p$. What remains to be estimated is the variance of detector noise $\sigma_d^2(p)$. Assuming that this variance is constant across the detector $[\sigma_d^2(p) = \sigma_d^2]$, we can estimate σ_d^2 by analyzing the variance of pixel distribution far away from the diffraction signal, where the contribution of the scattered electrons can be assumed to be close to zero. Once this variance is determined, $\sigma^2(p)$ can be calculated as $\sigma^2(p) = \sigma_d^2 + p$.

The reflection intensity is calculated as a sum of pixels in the reflection spot minus the background,

$$I = \sum_{N_s} p_i - (N_p/N_b) \sum_{N_b} p_i. \qquad (13)$$

Here the first sum runs over all N_s pixels considered by the integration program to belong to the spot, and the second sum runs over N_b pixels in the vicinity of the spot that are used to estimate the background. In the present case, the shape of diffraction spots was very similar across the diffraction pattern, and the spot area was estimated as a circle of a constant diameter centered at the peak position. The background was estimated from an annulus of pixels around the spot. The error propagation law then leads to the expression for $\sigma^2(I)$ [using the above expression for $\sigma^2(p_i)$]

$$\sigma^2(I) = \sum_{N_s}(p_i + \sigma_d^2) + (N_p/N_b)\sum_{N_b}(p_i + \sigma_d^2). \qquad (14)$$

References

Berg, B. S., Hansen, V., Midgley, P. A. & Gjønnes, J. (1998). *Ultramicroscopy*, **74**, 147–157.
Bethe, H. (1928). *Ann. Phys.* **392**, 55–129.
Birkel, C. S., Mugnaioli, E., Gorelik, T., Kolb, U., Panthoefer, M. & Tremel, W. (2010). *J. Am. Chem. Soc.* **132**, 9881–9889.
Cao, J., Guo, C. & Zou, H. (2009). *J. Solid State Chem.* **182**, 555–559.
Cheng, Y. F., Nüchter, W., Mayer, J., Weickenmeier, A. & Gjønnes, J. (1996). *Acta Cryst.* A**52**, 923–936.
Cowley, J. M. (1992). *Electron Diffraction Techniques*, Vols. 1 and 2. New York: Oxford University Press.
Cowley, J. M. & Moodie, A. F. (1957). *Acta Cryst.* **10**, 609–619.
Dorset, D. L. (1995). *Structural Electron Crystallography*. New York: Plenum Press.
Dudka, A. (2007). *J. Appl. Cryst.* **40**, 602–608.
Dudka, A. P., Avilov, A. S. & Lepeshov, G. G. (2008). *Crystallogr. Rep.* **53**, 530–536.
Edwards, D. D., Mason, T. O., Sinkler, W., Marks, L., Poeppelmeier, K. R., Hu, Z. & Jorgensen, J. (2000). *J. Solid State Chem.* **150**, 294–304.
Feng, F., Zhu, J. & Zhang, A. (2005). *Acta Cryst.* A**61**, 453–459.
Gemmi, M., Campostrini, I., Demartin, F., Gorelik, T. E. & Gramaccioli, C. M. (2012). *Acta Cryst.* B**68**, 15–23.
Gemmi, M., Klein, H., Rageau, A., Strobel, P. & Le Cras, F. (2010). *Acta Cryst.* B**66**, 60–68.
Gilmore, C. J., Marks, L., Grozea, D., Collazo, C. E., Landree, E. & Twesten, R. (1997). *Surf. Sci.* **381**, 77–91.
Gjønnes, J., Hansen, V., Andersen, S. J., Marioara, C. D. & Li, X. Z. (2003). *Z. Kristallogr.* **218**, 293–307.
Hadermann, J., Abakumov, A. M., Tsirlin, A. A., Filonenko, V. P., Gonnissen, J., Tan, H., Verbeeck, J., Gemmi, M., Antipov, E. V. & Rosner, H. (2010). *Ultramicroscopy*, **110**, 881–890.
Hirsch, P., Howie, A., Nicholson, R., Pashley, D. & Whelan, M. (1977). *Electron Microscopy of Thin Crystals*. Florida: Robert E. Krieger.
Humphreys, C. J. (1979). *Rep. Prog. Phys.* **42**, 1825–1887.
Iijima, S. (1991). *Nature (London)*, **354**, 56–58.
Jacob, D., Palatinus, L., Cuvillier, P., Leroux, H., Domeneghetti, C. & Cámara, F. (2013). *Am. Mineral.* Submitted.
Jansen, J., Tang, D., Zandbergen, H. W. & Schenk, H. (1998). *Acta Cryst.* A**54**, 91–101.
Jansen, J., Zandbergen, H. & Otten, M. (2004). *Ultramicroscopy*, **98**, 165–172.
Kilaas, R., Marks, L. D. & Own, C. S. (2005). *Ultramicroscopy*, **102**, 233–237.
Klein, H. (2011). *Acta Cryst.* A**67**, 303–309.
Leslie, A. G. W. (1999). *Acta Cryst.* D**55**, 1696–1702.
Marks, L. D. & Sinkler, W. (2003). *Microsc. Microanal.* **9**, 399–410.
Marks, L. D., Xu, P. & Dunn, D. N. (1993). *Surf. Sci.* **294**, 322–332.
Merli, M., Cámara, F., Domeneghetti, C. & Tazzoli, V. (2002). *Eur. J. Mineral.* **14**, 773–784.
Mugnaioli, E., Gorelik, T. & Kolb, U. (2009). *Ultramicroscopy*, **109**, 758–765.

Nuchter, W., Weickenmeier, A. & Mayer, J. (1998). *Phys. Status Solidi A*, **166**, 367–379.

Ogata, Y., Tsuda, K., Akishige, Y. & Tanaka, M. (2004). *Acta Cryst.* A**60**, 525–531.

Oleynikov, P. (2011). *Cryst. Res. Technol.* **46**, 569–579.

Own, C. J. (2005). PhD thesis, Northwestern University, Evanston, IL, USA.

Own, C. S., Marks, L. D. & Sinkler, W. (2006). *Acta Cryst.* A**62**, 434–443.

Palatinus, L. (2011). *PETS – program for analysis of electron diffraction data.* Institute of Physics of the AS CR, Prague, Czech Republic.

Palatinus, L., Klementová, M., Dřínek, V., Jarošová, M. & Petříček, V. (2011). *Inorg. Chem.* **50**, 3743–3751.

Petříček, V., Dušek, M. & Palatinus, L. (2006). *The crystallographic computing system JANA2006.* Institute of Physics, Prague, Czech Republic.

Phillips, W. C., Stanton, M., Stewart, A., Qian, H., Ingersoll, C. & Sweet, R. M. (2000). *J. Appl. Cryst.* **33**, 243–251.

Rozhdestvenskaya, I., Mugnaioli, E., Czank, M., Depmeier, W., Kolb, U., Reinholdt, A. & Weirich, T. (2010). *Mineral. Mag.* **74**, 159–177.

Self, P. G. & O'Keefe, M. A. (1988). *Calculation of diffraction patterns and images for fast electrons.* In *High-Resolution Transmission Electron Microscopy and Associated Techniques*, edited by P. R. Busek, J. M. Cowley & L. Eyring. Oxford University Press.

Sinkler, W. & Marks, L. (2010). *Z. Kristallogr.* **225**, 47–55.

Sinkler, W., Marks, L. D., Edwards, D. D., Mason, T. O., Poeppelmeier, K. R., Hu, Z. & Jorgensen, J. D. (1998). *J. Solid State Chem.* **136**, 145–149.

Sinkler, W., Own, C. S. & Marks, L. D. (2007). *Ultramicroscopy*, **107**, 543–550.

Spence, J. & Zuo, J. M. (1992). *Electron Microdiffraction.* New York: Plenum Press.

Spence, J. C. H. (1993). *Acta Cryst.* A**49**, 231–260.

Stadelmann, P. (2004). *JEMS, electron microscopy software.* CIME-EPFL, CH 1015 Lausanne, Switzerland.

Steeds, J. W., Bird, D. M., Eaglesham, D. J., McKernan, S., Vincent, R. & Withers, R. L. (1985). *Ultramicroscopy*, **18**, 97–110.

Stimpfl, M., Ganguly, J. & Molin, G. (1999). *Contrib. Mineral. Petrol.* **136**, 297–309.

Takayanagi, K., Tanishiro, Y., Takahashi, S. & Takahashi, M. (1985). *Surf. Sci.* **164**, 367–392.

Tarantino, S. C., Domeneghetti, M. C., Carpenter, M. A., Shaw, C. J. S. & Tazzoli, V. (2002). *Eur. J. Mineral.* **14**, 525–536.

Többens, D. M., Stüsser, N., Knorr, K., Mayer, H. M. & Lampert, G. (2001). *Mater. Sci. Forum*, **378**, 288–293.

Tsuda, K., Morikawa, D., Watanabe, Y., Ohtani, S. & Arima, T. (2010). *Phys. Rev. B*, **81**, 180102.

Tsuda, K., Ogata, Y., Takagi, K., Hashimoto, T. & Tanaka, M. (2002). *Acta Cryst.* A**58**, 514–525.

Tsuda, K. & Tanaka, M. (1999). *Acta Cryst.* A**55**, 939–954.

Vainshtein, B. K. (1964). *Electron Diffraction Structure Analysis.* Oxford: Pergamon Press.

Vincent, R. & Midgley, P. A. (1994). *Ultramicroscopy*, **53**, 271–282.

Waterman, D. & Evans, G. (2010). *J. Appl. Cryst.* **43**, 1356–1371.

Weickenmeier, A. & Kohl, H. (1991). *Acta Cryst.* A**47**, 590–597.

White, T. A., Sergio Moreno, M. & Midgley, P. A. (2010). *Z. Kristallogr.* **225**, 56–66.

Yim, W. M. & Paff, R. J. (1974). *J. Appl. Phys.* **45**, 1456–1457.

Zhang, X. B., Zhang, X. F., Amelinckx, S., Van Tendeloo, G. & Van Landuyt, J. (1993). *Ultramicroscopy*, **54**, 237–249.

Zuo, J. & Spence, J. (1991). *Ultramicroscopy*, **35**, 185–196.

Zuo, J. M. (1993). *Acta Cryst.* A**49**, 429–435.

Zuo, J. M., Spence, J. C. H., Downs, J. & Mayer, J. (1993). *Acta Cryst.* A**49**, 422–429.

Zuo, J. M. & Weickenmeier, A. L. (1995). *Ultramicroscopy*, **57**, 375–383.